Atomic resolution non-contact atomic force microscopy of clean metal oxide surfaces

2010 J. Phys.: Condens. Matter 22 263001

(http://iopscience.iop.org/0953-8984/22/26/263001)

IOP Publishing Journal of Physics: Condensed Matter

J. Phys.: Condens. Matter **22** (2010) 263001 (23pp) doi:10.1088/0953-8984/22/26/263001

TOPICAL REVIEW

Atomic resolution non-contact atomic force microscopy of clean metal oxide surfaces

J V Lauritsen[1] **and M Reichling**[2]

[1] Interdisciplinary Nanoscience Center, Aarhus University, Denmark
[2] Fachbereich Physik, Universität Osnabrück, Germany

E-mail: jvang@inano.au.dk and reichling@uos.de

Received 9 February 2010
Published 24 May 2010
Online at stacks.iop.org/JPhysCM/22/263001

Abstract

In the last two decades the atomic force microscope (AFM) has become the premier tool for topographical analysis of surface structures at the nanometre scale. In its ultimately sensitive implementation, namely dynamic scanning force microscopy (SFM) operated in the so-called non-contact mode (NC-AFM), this technique yields genuine atomic resolution and offers a unique tool for real space atomic-scale studies of surfaces, nanoparticles as well as thin films, single atoms and molecules on surfaces irrespective of the substrate being electrically conducting or non-conducting. Recent advances in NC-AFM have paved the way for groundbreaking atomic level insight into insulator surfaces, specifically in the most important field of metal oxides. NC-AFM imaging now strongly contributes to our understanding of the surface structure, chemical composition, defects, polarity and reactivity of metal oxide surfaces and related physical and chemical surface processes. Here we review the latest advancements in the field of NC-AFM applied to the fundamental atomic resolution studies of clean single crystal metal oxide surfaces with special focus on the representative materials $Al_2O_3(0001)$, $TiO_2(110)$, ZnO(1000) and $CeO_2(111)$.

(Some figures in this article are in colour only in the electronic version)

Contents

1. Introduction 1
2. Experimental aspects of NC-AFM 3
   2.1. Fundamental operation of NC-AFM 3
   2.2. Interpretation of atom-resolved NC-AFM images 4
   2.3. Preparation of metal oxide surfaces for NC-AFM experiments 4
3. Rutile $TiO_2(110)$ 5
4. α-$Al_2O_3(0001)$ 8
5. Polar ZnO(0001) surfaces 11
6. $CeO_2(111)$ 15
7. Perspectives on future NC-AFM research on metal oxide surfaces 17
Acknowledgments 19
References 19

1. Introduction

The group of *metal oxide materials* exhibits in general a very diverse range of physical and chemical properties, which are essential to many modern technologies. Metal oxides are, e.g., an integral part of electronics, actuators, chemical sensors, heterogeneous catalysts, and they form the basis for novel functional thin film applications, data storage devices as well as tissue engineering and biocompatible implant technologies [1–3]. Transparent, wide band-gap metal oxides present promising new solutions in solar cell materials, photonic devices, high-temperature electronics and photocatalytic applications [4, 5]. Recent advances in the synthesis of nanostructured metal oxides have in particular highlighted the possibilities for designing new materials with unique functional properties [6–8]. Many important

Table 1. Literature overview of atomically resolved NC-AFM studies on metal oxides surfaces up to the year 2009.

Oxide	Surface	References	Additional techniques[a]
TiO_2	(110)-1× 1	[23–39]	STM, KPFM
	(110)-*n*× 1	[40–42]	STM
	(011)-*n*× 1	[43]	STM
	(100)	[26]	STM
Al_2O_3	(0001)-$\sqrt{31} \times \sqrt{31}$R9°	[21, 44, 45]	
	(0001)	[46]	
	Film/NiAl(111)	[13, 47, 48]	STM
	Film/NiAl(110)	[49–51]	STM
ZnO	(0001)-Zn	[52, 53]	
	(0001)-O	[54]	
CeO_2	(111)	[55–64]	
MgO	(001)	[65–67]	
	Film/Ag(001)	[68–70]	
$SrTiO_3$	(100)	[71, 72]	STM
SnO_2	(110)	[73]	STM
NiO	(100)	[74–79]	MxFM
MoO_3	(010)	[80]	
Others	Spinels, mica, films	[81–84]	

[a] Abbreviations: STM: scanning tunnelling microscopy [85], MxFM: magnetic exchange force microscopy [77], KPFM: Kelvin probe force microscopy [86].

phenomena such as nucleation and growth, adhesion, diffusion and corrosion are directly linked to the fundamental surface properties of the metal oxide [9], and it has become clear that a more advanced utilization of metal oxides in the above-mentioned applications urgently requires detailed, fundamental knowledge of *the surface structure of the metal oxide*. However, whereas the bulk geometric and electronic structure of many metal oxides have been characterized during the course of many years and are now fairly well understood, the surface structure and properties of many metal oxides remain a big puzzle. The major reasons for this are the complexity of many oxide surfaces and the fact that a large fraction of the common metal oxides are, in the clean state, electrical insulators or poorly conducting semiconductors where the usually applied electron or ion based surface sensitive imaging, spectroscopy and diffraction tools provide only limited access to conclusive atomic-scale insight into the surface structure. Consequently, significant gaps exist in our knowledge of the surface properties even for very commonly used monometallic oxides such as TiO_2, SiO_2, ZnO, CeO_2 and Al_2O_3. Many of these gaps can be closed by high-resolution imaging by scanning probe techniques utilizing a sharp, ideally atomically well-defined tip probing the surface while rastered across the surface [10].

Scanning tunnelling microscopy (STM) has been a phenomenally successful surface science tool in recent years and STM studies have provided atomistic insight into the surface structure of a wealth of metals and conducting materials (see e.g. [11]), and also semiconducting oxides such as TiO_2. However, as the technique is based on electrons flowing freely to establish a tunnelling current between the tip and the surface, STM is not applicable to insulators. In the context of metal oxide research, an impressive amount of STM work has been presented on ultra-thin oxide films [12] allowing charge transfer through the film and thus overcoming the conductivity problem, but it has been realized in several cases that ultra-thin films lead to specific charge transfer effects or the stabilization of oxide structures which are different from any bulk properties (see e.g. [13–16]). The atomic force microscope (AFM), which is the technique treated in this review, is related to the STM, but instead of relying on the detection of a tunnelling current, the AFM measures the small forces acting between the tip and the surface. The force fields probed by AFM are ubiquitous and this makes the AFM a universal tool for nanoscale investigations of surfaces in liquids, air and under vacuum conditions. Owing to recent tremendous progress in developing the NC-AFM technique for atomic resolution imaging and manipulating surfaces [17–20], insulating metal oxide surfaces can now be studied in their atomic details at the same level as conducting materials are studied by STM. Having access to the real space atomic structure of insulating oxides allows us to address the structure and nanoscale properties of single defects, edges and other morphological features, as well as to monitor single atoms, molecules and individual nanoclusters on the oxide surface at a level not accessible with any other technique. Apart from the deep fundamental insight gained, a detailed analysis of defects on metal oxide surfaces and the adhesion of molecules and clusters is of relevance for understanding and controlling functionality in basically every application of metal oxides. Our expectation is, therefore, that in the coming years NC-AFM and derived techniques, such as Kelvin probe force microscopy (KPFM), will become increasingly important tools in the field of metal oxide research, as they have the potential to greatly advance the fundamental understanding of important insulating metal oxide surfaces. It took five years to obtain atomic resolution on a truly insulating oxide, namely $Al_2O_3(0001)$ [21], after the first successful demonstration of atom-resolved NC-AFM obtained on the semiconductor Si(111) 7 × 7 [22]. However, during the following decade, the field has expanded rapidly. In table 1 we provide a comprehensive overview of articles reporting

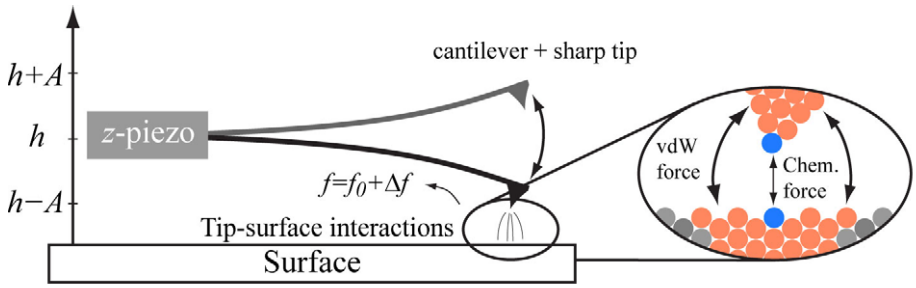

Figure 1. Schematic illustration of the working principle of AFM applied in the dynamic mode, where the cantilever is oscillated at frequency f. The illustration on the right is a magnified view of the tip apex at its closest approach.

on atomic resolution NC-AFM measurements on a variety of metal oxides surfaces.

The purpose of this review is to provide an overview of metal oxide studies conducted with the NC-AFM, to demonstrate the strength of NC-AFM imaging and to introduce four prototype metal oxide systems, namely TiO_2, Al_2O_3, ZnO and CeO_2, each highlighting a different aspect of oxide research. In section 3, we discuss the (110) surface of rutile TiO_2, providing a splendid example of the rich variety of contrast features that can be obtained in NC-AFM imaging, each revealing a certain aspect of the surface structure. The truly insulating oxide α-Al_2O_3 was the first case where NC-AFM excelled in providing atomic-scale information on the high-temperature reconstructed (0001) surface [21]. In section 4, we demonstrate how NC-AFM can reveal most detailed atomic structures providing the basis for a complete understanding of this most complex surface. Section 5 is devoted to the polar faces (0001) and $(000\bar{1})$ of the poorly conducting oxide ZnO, where NC-AFM imaging greatly contributes to the understanding of charge compensation mechanisms for the stabilization of the polar faces. The studies on $CeO_2(111)$, reviewed in section 6, highlight the ability of NC-AFM to reveal structural details of surface defects that are important to identify for an understanding of the surface chemistry of this material, which is most relevant in heterogeneous catalysis. We restrict the review to bare surfaces of metal oxides but envisage the extension of this field into the world of complex functional nanosystems, involving oxide surfaces and interfaces, in section 7.

2. Experimental aspects of NC-AFM

2.1. Fundamental operation of NC-AFM

The atomic force microscope belongs to the group of scanning probe microscopes (SPM), which share the common principle that a sharp tip is brought into close proximity to a surface and is scanned across the surface to measure a 2D map of a specific property related to the tip–surface interaction. In NC-AFM, under ideal conditions, forces with a magnitude of typically a few nanonewtons and below are measured with a lateral resolution down to the single atom level. For the measurements of minute interactions arising from the force field of the surface, the AFM, in its most common form, uses an 'atomically sharp' silicon tip fixed at the free end of a flexible cantilever with the other end clamped (figure 1). As tip and surface are placed within close proximity, forces arise and, depending on the magnitude of these forces, the cantilever will respond by bending according to Hooke's law. Usually, the flexing of the cantilever is measured with high precision by reflecting a laser beam from the back-side of the cantilever onto a position sensitive photodiode (PSD), thus achieving a very high mechanical amplification of the cantilever motion.

For the high-resolution measurements relevant to this review, the AFM is operated in the *dynamic mode*, where the cantilever is excited to oscillation at its resonance frequency and the dynamic response of the oscillating cantilever is measured [87] instead of the static deflection of the cantilever as for conventional AFM [88] (figure 1). In the so-called non-contact AFM mode (NC-AFM), the interaction of the tip with the surface is restricted to an overall attractive force, in contrast to the tapping mode [88, 89], where contrast formation is mainly due to repulsive forces. The NC-AFM operation is preferred for high-resolution AFM since it is non-destructive, and it is the only mode capable of *genuine atomic resolution* of, e.g., single atomic defects and adsorbates [17, 18, 20, 90]. NC-AFM force detection is mostly facilitated by the frequency modulation scheme, where the cantilever is excited at its first mechanical resonance (typically 50–300 kHz) at a constant amplitude (typically 5–30 nm), and the primary measurement signal is a shift in the cantilever resonance frequency. The forces arising between tip and surface as the tip is moved towards the surface cause this shift, further on referred to as Δf, frequency shift or detuning in the resonance frequency relative to the frequency f_0 of the freely oscillating cantilever. As the tip is raster-scanned across the surface, variations in the detuning signal are recorded and used to generate the NC-AFM image, either as the direct imaging signal (constant height image) or as a feedback loop signal controlling the tip–surface distance to maintain a pre-set detuning (constant detuning image). In the latter mode, the tip traces the surface on a *contour of constant frequency shift*, and the changes in tip–surface distance controlled by the feedback loop are used as the imaging signal, thus generating a 'topographic' image of the surface. All images presented in this review are obtained by a non-contact force microscope operated with frequency modulation under ultra-high vacuum (UHV) conditions. Other measurements were, however, taken with a tuning fork sensor, which is an alternative force detection scheme [17]. It should be noted that the NC-AFM technique is not only capable of imaging but also of high-precision manipulation of individual

atomic species on a solid surface [19]. This capability, originally developed for semiconducting surfaces, has recently been transferred to an insulating surface [91], and it can be foreseen that in future atomic-scale manipulation will also play a major role in oxide surface research performed with the NC-AFM.

2.2. Interpretation of atom-resolved NC-AFM images

Images in non-contact AFM are generated by the forces active during the oscillation cycle of the tip. The total force acting between the tip and surface is composed of several contributions which can be broadly categorized into long-range and short-range forces. Long-range forces are determined by the macroscopic shape of the tip, where the major contributions are normally *van der Waals forces* and *electrostatic* forces [92, 90]. These forces are significant for a tip–surface distance of up to ∼100 nm, and, depending on the tip sharpness, they often define the lateral resolution of the AFM with respect to imaging corrugated objects such as particles, pits and step edges. The atomic resolution capability of NC-AFM is, on the other hand, attributed to short-range forces acting between a nano-sized apex of the tip (ideally a single atom) and the surface (see magnified view in figure 1). Atomic resolution in NC-AFM is intuitively understood by the strong localization of the short-range forces existing for this geometry. Short-range forces have a significant strength only when the tip is close to its point of closest approach (<1 nm) to the surface, and mostly reflect a 'chemical' interaction between the outermost atom(s) protruding from the tip and the surface. For this reason, short-range forces are often referred to as 'chemical' forces, although they principally can both have an attractive and a repulsive character. Any atomic corrugation is, therefore, determined by the nanoapex on the tip and its affinity to interact with the atomic species at a given tip–surface distance. Due to the combination of long and short-range forces, the apparent contrast in NC-AFM should generally be interpreted as a superposition of the geometric structure of the surface and a chemical contribution reflecting the bonding affinity of the tip apex.

For short-range tip–surface interactions reflecting covalent bonding, for instance scanning with a clean silicon tip on silicon, the 'chemical' contrast typically closely reflects the geometry of the surface unless a contrast inversion is invoked by special experimental conditions [93]. For ionic surfaces, however, the chemical contrast can be very tip dependent and a specific type of force contribution may entirely dominate the contrast seen in atom-resolved NC-AFM images, as has been reported for compound surfaces such as KBr [94], NaCl [95] and CaF_2 [96], where preferentially a single type of ionic sublattice creates bright contrast features. This is also observed for oxide surfaces, as will be outlined for the example of rutile $TiO_2(110)$ in section 3. It is, therefore, generally not valid to interpret atom-resolved NC-AFM images as pure topography maps of the surface, and image interpretation should always take into account the particular interaction of the nanoapex, which is unfortunately generally in a rather poorly defined structural and chemical state due to contact with the surface or adsorption/desorption events. From a theoretical point of view, the basic principles of (topographic) atomic resolution in NC-AFM are rather well understood; much of the theoretical framework needed to describe contrast formation on insulating surfaces has been developed in a series of papers describing quantitative imaging on fluorite [96–98]. A key issue in these studies is to find valid models for the nano-asperity determining atomic contrast formation, as the atomic structure and stoichiometry of tips used in experiments is not known *a priori* [99]. It is beyond the scope of this review to account for an in-depth discussion of the possibilities and the current state-of-the-art in this field, but we refer to references [92, 100, 101] for an overview.

2.3. Preparation of metal oxide surfaces for NC-AFM experiments

Performing high-resolution NC-AFM experiments on metal oxides relies to a large extent on good and reproducible sample preparation. The studies discussed in this review are performed on single crystal metal oxide surfaces prepared in an ultra-high vacuum (UHV) environment. Preparation in UHV offers the possibility to prepare a clean metal oxide surface under well-controlled conditions. Many metal oxides exhibit a very complicated surface phase diagram (see e.g. [45, 102–105]), especially for surfaces that contain multivalent cations (e.g. Ti [106]), and the specific stoichiometry and surface structure critically depends on the temperature and the presence of reacting gases such as H_2, O_2, H_2O during preparation. The UHV environment offers the means to control the surface state very reproducibly and, when relevant, investigate phase transitions or study reactions with dosed gases on the surface. UHV is, therefore, often considered to be mandatory in order to be able to systematically compare experiments on metal oxides surface. One route of sample preparation for NC-AFM experiments is by cleaving [107–109] metal oxide crystals in air or *in vacuo* along weakly bound crystallographic planes, followed by heating in UHV, a procedure typically used to produce a clean MgO(001) surface [67]. More often, the preparation of oxides is based on cycles of surface cleaning with ion bombardment and annealing in UHV or an oxidizing atmosphere to restore a stoichiometric, atomically well-ordered surface. Creating a planar surface after sputtering often requires temperatures in excess of 800 °C, sometimes even approaching 1400 °C, which has to be kept in mind when constructing a sample holder to support the crystal during preparation. Annealing in oxygen may be necessary to restore the surface stoichiometry if preferential sputtering results in an excessive depletion of oxygen at the surface. As a typical example, we show in figure 2(a) a large-scale NC-AFM image of an $Al_2O_3(0001)$ surface prepared by numerous sputter/annealing cycles, where annealing was performed at a temperature of 1200 °C in oxygen at 10^{-7} mbar.

For preparation purposes, a check of surface cleanliness and a measurement of the surface stoichiometry (metal to oxygen ratio) can conveniently be performed, e.g., by x-ray photo-electron spectroscopy (XPS) and implementing an

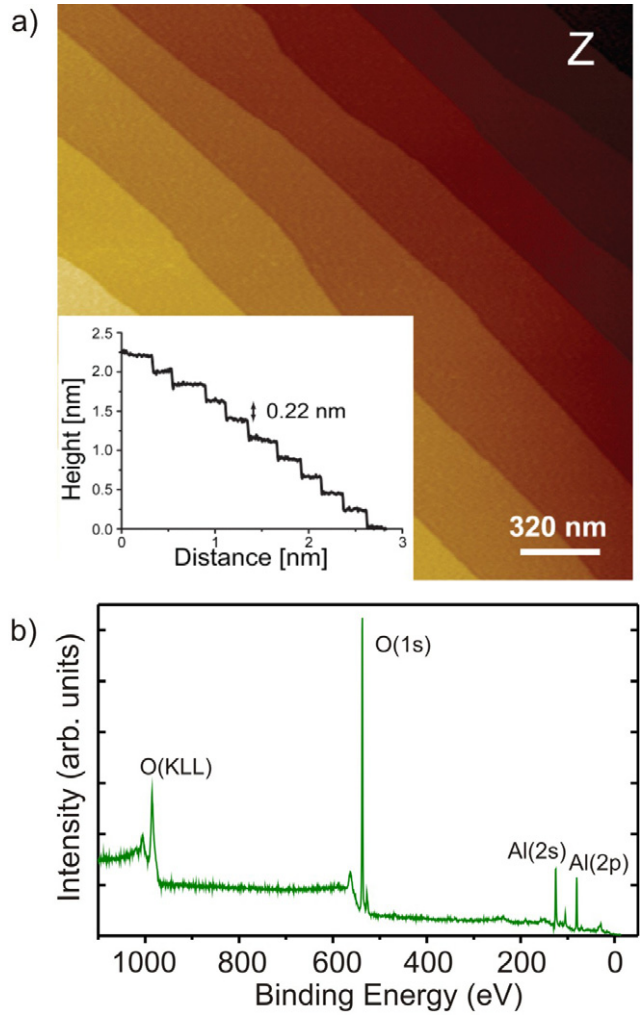

Figure 2. (a) Large-scale NC-AFM image showing the topography of $Al_2O_3(0001)$ prepared by high-temperature annealing under UHV conditions. The inset is a line scan showing the step height. (b) XPS spectrum recorded on the clean $Al_2O_3(0001)$ surface. No charge compensation was applied in this case.

electron flood gun for charge compensation on insulators, see figure 2(b).

3. Rutile $TiO_2(110)$

The surfaces of titaniumdioxide (also called titania, TiO_2) are indisputably the most studied metal oxide surfaces from a fundamental point of view, in part because of the major importance of titania as a photocatalyst [110, 111] and as an active support for metal catalysts [112, 113], but also because titania is often considered as a prototypical system for reducible transition metal oxide surfaces [114]. Equally important seems the fact that pristine and non-conducting TiO_2 is readily transformed by heating under vacuum conditions to a slightly reduced TiO_2 state, which increases the conductivity enough to apply the full range of standard surface science tools, including the STM. In particular, the rutile $TiO_2(110)$-(1×1) surface has attracted much attention because this surface is the most stable facet of rutile TiO_2, and in a number of recent studies the structure of this surface and its prevalent defects under typical UHV conditions have been revealed in impressive atomic detail. An exhaustive review of the surface science of TiO_2 and was given by Diebold in 2003 [114] while more recent STM studies are treated in e.g. [10, 115, 116].

Although not a real insulator, a number of recent NC-AFM studies have focused on imaging the $TiO_2(110)$-(1×1) surface in atomic detail. The main interest in NC-AFM studies of TiO_2 surfaces stems from the fact that this well-characterized surface offers an excellent model system for studying the details of atomic NC-AFM resolution on metal oxides in general and for testing the modelling of the corrugations using various model tip terminations [117, 118]. In particular, the importance of the exact tip termination for imaging the sublattices of ionic materials and surface defects is revealed in a very clear manner for $TiO_2(110)$. As illustrated in the ball model in figure 3(a), the clean $TiO_2(110)(1\times1)$ surface prepared under UHV conditions is known to expose a surface structure consisting of alternating rows of two-fold coordinated bridging oxygen atoms (O(2c), formally charged O^{-2}) and adjacent rows of five-fold coordinated Ti atoms (Ti(5c), formally charged Ti^{+4}) located ∼120 pm below the O rows [119]. This structure is clearly visible in atom-resolved NC-AFM images as a rippled structure on the surface, reflecting the repetition of rows separated by a 6.5 Å distance, as shown in figure 3(b) [23, 26, 27, 30].

From the corrugated geometry of the surface one would intuitively interpret the NC-AFM images by assigning the bright rows to the protruding O atoms and the darker rows to the Ti atoms located in the troughs. However, a detailed analysis of the location of defects imaged in the NC-AFM images in a recent study by Lauritsen *et al* [27] revealed that this is not a generally valid assignment and that the qualitative contrast seen with NC-AFM is very sensitive to the specific state of the tip apex [27, 29, 30, 118]. The TiO_2 surface, when prepared under UHV conditions, always exposes a small population of defects, as also seen in the NC-AFM image in figure 3(b). These point-like defects have been exceptionally well characterized by STM and other techniques in the recent literature [116, 120, 121], and are found to originate from oxygen vacancies (O-vac) formed under thermal treatment by removal of single bridging O atoms on the $TiO_2(110)$ surface (figure 3(a)). The O vacancies are very reactive towards water, and even under very good UHV conditions it has been demonstrated that water readily adsorbs from the residual gas and dissociates in the O vacancies [120]. The water splits off one H, which adsorbs on a neighbouring bridging O atom, leading to the formation of a double OH (dOH), consisting of two neighbouring OH groups (see ball model in figure 3(a)). On a timescale of a few hours it has also previously been visualized how the double OH groups eventually spilt by water-mediated diffusion into single OH groups (sOH) [30, 120, 122]. Thus, at any stage after preparation, the $TiO_2(110)$ surface exposes varying populations of these three types of defects, O-vac, dOH and sOH, ending up in a situation where the surface is partially hydroxylated with sOH groups.

Figures 4(a)–(c) shows three types of atom-resolved NC-AFM images from the studies in [27, 30] of the same

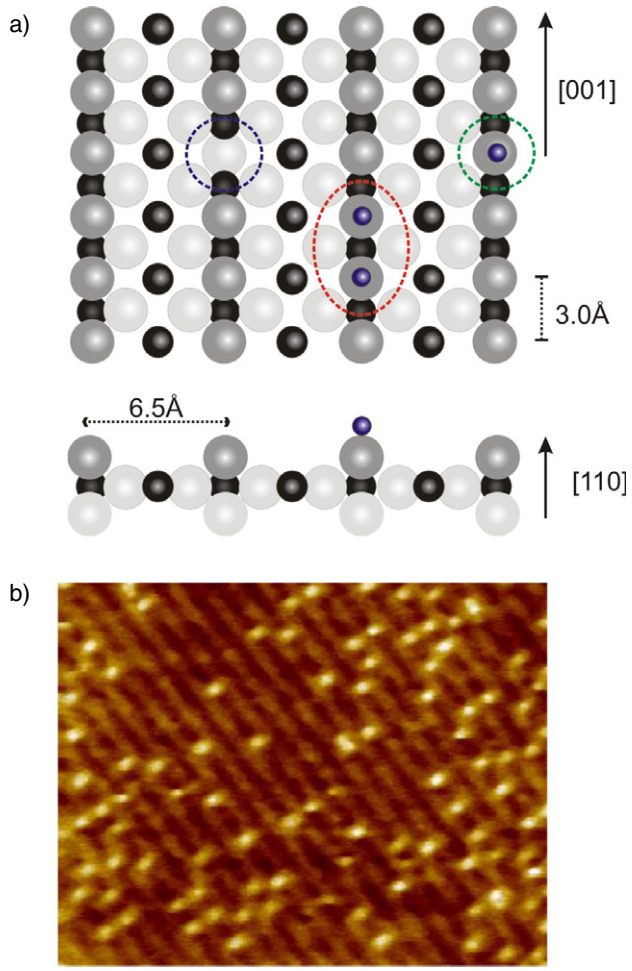

Figure 3. (a) Ball model of the rutile $TiO_2(110)(1 \times 1)$ surface, shown in top view (upper) and side view (lower), respectively. The surface exposes rows of bridging O(2c) atoms (grey) protruding above a plane of three-fold coordinated oxygen atoms, and rows of Ti(5c) atoms (black) located geometrically lower. A lighter grey tone is used for O in the subsurface region. Also shown in the ball model are the three predominant types of defects present on $TiO_2(110)$ after UHV preparation: an oxygen vacancy (O-vac, i.e. a missing O(2c) atom), double OH groups (dOH) formed by water dissociation in the O-vac, and single OH groups (sOH), respectively. Hydrogen atoms are represented by smaller dark balls. (b) Typical large-scale NC-AFM image of the $TiO_2(110)$–(1×1) surface (150×200 Å^2). Adapted with permission from [30]. Copyright 2007, American Physical Society.

$TiO_2(110)$ surface just before full hydroxylation was achieved. In the first image in figure 4(a) the characteristic row structure of $TiO_2(110)$ is again clearly visible, and as indicated by the squares and circles the TiO_2 surface in this state exposes all three types of point-like defects. Oxygen vacancies were identified as rather faint protrusions located in between the bright rows (squares), whereas sOH and dOH groups are visible as rather bright protrusions with an elongation, matching either a single or a double periodicity along the O rows, also placed in between the rows. However, as shown in figures 4(b) and (c), two entirely different modes of NC-AFM images could be obtained on the very same surface after a slight change of the tip. In figure 4(b) the defects are still imaged as protrusions, but in contrast to figure 4(a) they are located directly on the bright rows. In figure 4(c) the contrast is inverted compared to figure 4(a), with sOH groups imaged as depressions located on the bright rows. In each case the resolved position of the defects allows an unambiguous determination of the Ti and O sublattices, since all three types of defects are located on the O rows (figure 3(a)).

The emergence of the three different types of contrast in figures 4(a)–(c) was explained by variations in the nature of the short-range chemical interaction force between tip and surface (figure 1). In a situation where ionic forces dominate the short-range tip–surface interactions, a negatively charged tip apex (e.g. O-terminated) will preferentially image electropositive species (Ti rows) as bright, whereas an electropositive tip (e.g, Ti-terminated) qualitatively inverts the situation and preferentially interacts with electronegative species (O rows) and images O–H groups as a depression due to the repulsion of a positive tip with the H. This corresponds to the experimental images shown in figures 4(a) and (c), which were referred to as hole mode and protrusion mode, respectively. The last option in figure 4(b) was referred to as *neutral mode imaging*, since the topographic appearance with both O rows and OH groups protruding from the surface suggests that ionic bonding is not predominant. Instead the interaction between a 'neutral' tip gives a covalent character to the short-range force, and contours of an NC-AFM image then closely reflect the surface topography.

The assignment of the contrast in the three modes and the appearance of the defects were investigated in extensive experiments and simulations that confirmed the origin of the contrast differences to variations in the charged state of the tip [30]. Figures 5(a)–(f) show NC-AFM simulations for O-vac, sOH and dOH, respectively, performed for a model tip (MgO-cube) consisting either of a positively charged (Mg^{2+}) or a negatively charged (O^{2-}) nanoapex. For both tips, the qualitative contrast matches the experiment very well, which shows that NC-AFM imaging is in general a reliable tool for the discrimination and identification of defects and adsorbates. In extension of these studies, the interplay between experiment and simulations in [30] also showed, in terms of detuning versus distance curves and images recorded at different detuning set points, that the qualitative appearance and relative contrast associated with all three defects on $TiO_2(110)$ were fixed for the typical closest tip–surface approaches, which are controlled experimentally by the amplitude and Δf-feedback setting.

Controlled modification of the tip apex structure and chemistry in NC-AFM has only been demonstrated in exceptional low-temperature cases [123], and generally the tip apex of an AFM tip cannot be controlled to give a desired type of contrast. However, as shown in figure 6 it is possible to provoke tip changes by scanning close to the surface or in other ways induce a restructuring of the tip apex. Figure 6 depicts an AFM image during a tip change, resulting in a change from hole mode to protrusion mode imaging. At the point indicated by the lower horizontal white dashed line, the tip probably came in close contact with the surface, causing the atoms forming the tip apex to rearrange, resulting in an

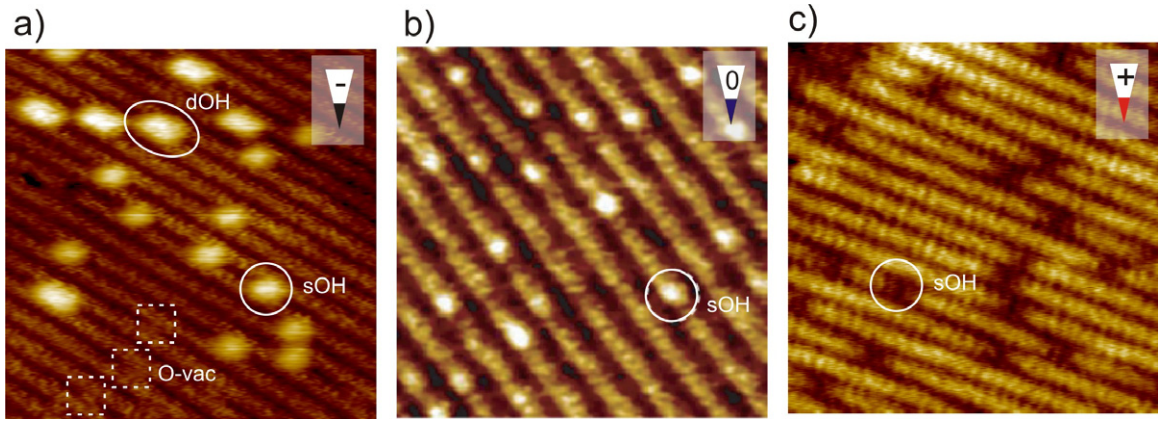

Figure 4. Three atom-resolved non-contact AFM images of the same $TiO_2(1 \times 1)$ surface imaged under the same conditions but with different AFM tips. (a) Image recorded with a negative tip termination (protrusion mode). Size: 100×100 Å^2. $\Delta f = -14.4$ Hz. (b) A neutral tip termination (neutral mode) 100×100 Å^2, $\Delta f = -53$ Hz (c) and positive tip termination (hole mode), 73×93 Å^2, $\Delta f = -36.1$ Hz and $U_{\text{bias}} = +1.70$ V. Figures reproduced with permission from [27, 30]. Copyright 2006, IOP Publishing and 2007, the American Physical Society, respectively.

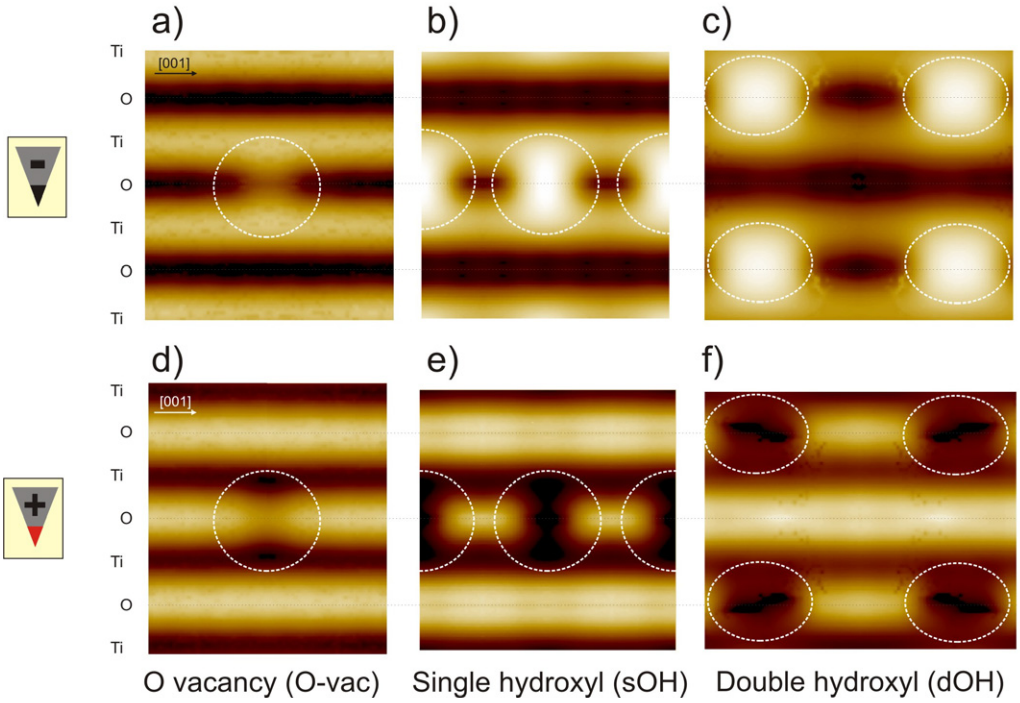

Figure 5. Simulations of the non-contact AFM contrast for the three types of defects on a $TiO_2(110)$ surface. (a)–(c) Simulated at a tip surface distance of ∼4.5 Å for a negatively terminated tip apex (protrusion mode). (d)–(f) Simulated at a tip surface distance ∼4.5 Å for a positively terminated tip apex (hole mode). Reproduced with permission from [27]. Copyright 2006 IOP Publishing.

unstable tip. This event produced a fuzzy contrast for a short period (a few line scans), but relatively quickly the tip apex stabilized, and good imaging contrast was recovered. The graph to the left in figure 6 shows a cross-sectional scan of the NC-AFM image, parallel to the slow scan direction indicated by the vertical white solid line. It is evident that the change in imaging contrast is associated with a 'tip jump', where the feedback loop instantly retracts the tip, caused by an alteration of the outermost tip atoms. The change in height is, however, relatively small, only ∼110 pm, indicating that the change in the tip apex conformation takes place on the *single atom level*, and most likely a single oxygen anion has been picked up from the surface and added to the tip apex, causing the 'tip-jump', and switching the polarity of the tip apex atom from electropositive to electronegative.

Previously, Onishi and co-workers demonstrated another promising method for identification of sublattice sites on $TiO_2(110)$ with NC-AFM by use of suitable probe molecules dosed to the vacuum, leading to the formation of formate and acetate with a known affinity for surface Ti sites [24, 25, 124]. An important outcome of the recent NC-AFM studies of the role of the tip for atomic contrast on TiO_2 is, however,

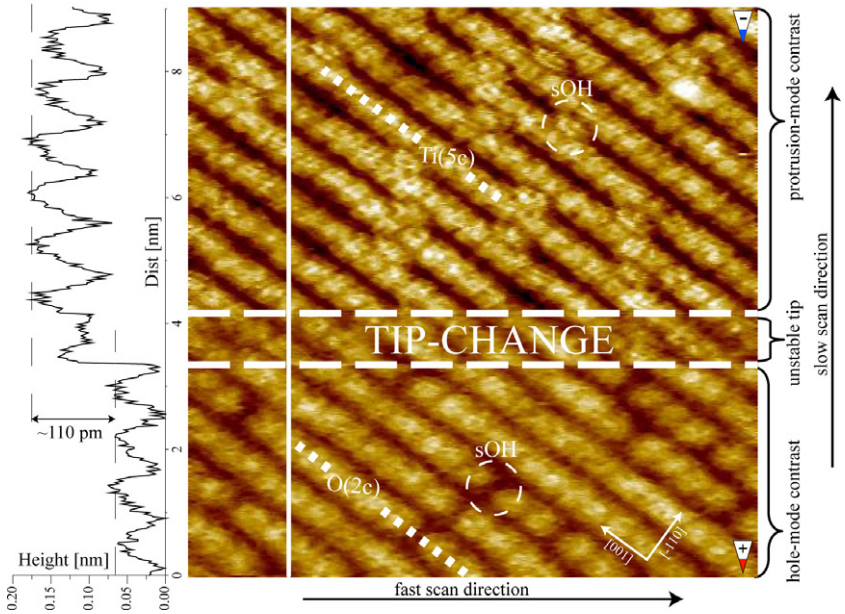

Figure 6. Atomically resolved constant detuning NC-AFM image of the fully hydroxylated $TiO_2(110)$ surface showing a tip change resulting in a change of contrast. White dashed circles and dotted lines indicate the positions of sOH, O(2c) and Ti(5c) rows. To the left is shown a cross-section taken along the solid white vertical line of the raw-data image. $\Delta f = -306$ Hz, $A_{p-p} \sim 20$ nm, size $= 90 \times 90$ Å^2. Reproduced with permission from [30]. Copyright 2007, the American Physical Society.

the realization that relatively simple knowledge on the charged state of the AFM tip can facilitate convenient chemical identification of surface defects and adsorbates, as demonstrated in [27] in the case of TiO_2. This is a strategy that was recently used also to identify defects on other ionic surfaces [95]. It is however important to emphasize that more realistic tip models beyond the simple MgO-cube are needed for a more accurate quantitative analysis of the corrugations seen in the NC-AFM experiment. As demonstrated in [32] the determination of a very accurate model of the tip nanoapex can be achieved for TiO_2 by recording simultaneously the STM signal (tunnelling current) and matching both the NC-AFM and STM corrugations. Very recently, a further theory/simulation study showed that a Si tip terminated by an OH group can also explain the neutral mode imaging shown in figure 4(b) [39]. The same study also included a discussion of a fourth, rare type of contrast of TiO_2 ('all-inclusive' mode) showing resolution on both Ti and O rows which could be reproduced in detail using a polarized two-atom tip that exposed both O and Si atoms from the tip apex. Rahe *et al* [125] recently discussed a different effect, where contrast inversion could be seen for adsorbates on TiO_2 even without a tip change. In that case a protruding adsorbate would appear as protrusion with a sharp depression inside. This appearance was attributed to an image artefact, and was explained by a sudden switch into the repulsive region of the short-range forces when probing a protrusion with NC-AFM with a relatively slow feedback loop.

The other surfaces of TiO_2 have been investigated to a much smaller extent both in general and with NC-AFM (see table 1) [114, 126], which is probably due to the challenges involved in reproducible preparation of flat and clean surfaces. In addition, TiO_2 also exists in different polymorphic forms, of which *anatase* TiO_2 is the most important form, generally obtained for nanoporous TiO_2 powders such as in heterogeneous catalysts or in photocatalytic applications. Such surfaces tend to be less conducting than the $TiO_2(110)$-(1×1) and there is no doubt that NC-AFM offers the future possibility to advance the fundamental understanding of other interesting titania surfaces.

4. α-$Al_2O_3(0001)$

Aluminium oxide (also called alumina, Al_2O_3) is a versatile metal oxide used in numerous technological applications, such as substrates for microelectronic devices and for the growth of novel functional thin films and coatings to support materials for a variety of high-surface-area heterogeneous catalysts [127]. Al_2O_3 is a robust insulator with a band-gap exceeding 8 eV and, as for most other insulators, traditional surface science techniques relying on the detection of charged species have had limited success in providing detailed structural insight into alumina surfaces. The (0001) surface of corundum α-Al_2O_3 has attracted much attention since it is the most stable polymorph of Al_2O_3 and the (0001) aluminium oxide surface is often used as a substrate for, e.g., thin film growth. Early structural information on the α-$Al_2O_3(0001)$ surface was obtained by low energy electron diffraction (LEED) [128–130] and grazing incidence x-ray diffraction (GIXD) [131–133]. The structure of the $Al_2O_3(0001)$ surface and the interaction of adsorbates and metals has also been extensively studied using various theoretical methods, including density functional theory [103, 134–140]. However, the lack of appropriate experimental tools means that even for clean α-Al_2O_3 surfaces a detailed atomic-scale characterization is still missing [141], and in this regard NC-AFM stands out as the appropriate tool

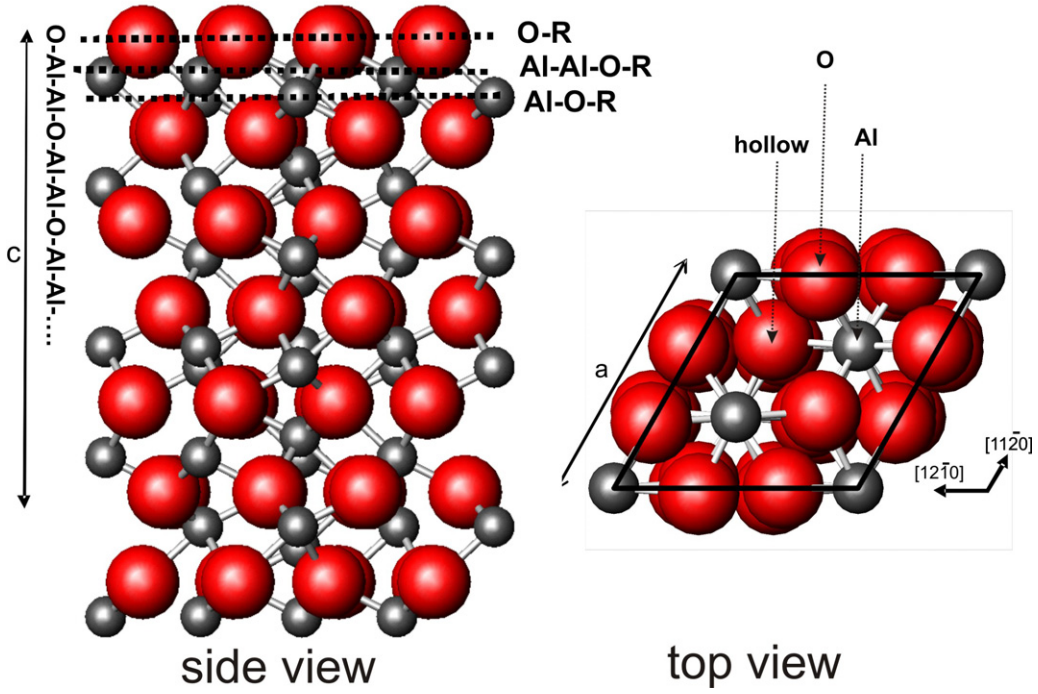

Figure 7. Left: side view of the α-Al_2O_3 crystal structure. Lines indicate the possible cleavage planes of the (0001) surface, $c = 12.8$ Å. Right: top view of the Al–Al–O–R termination of $Al_2O_3(0001)$, $a = 4.75$ Å. The Al–Al–O–R is the substrate for the Al overlayer in the $\sqrt{31} \times \sqrt{31}$R°9 surface reconstruction and exposes three different groups of sites available for stacking of the Al overlayer, as indicated by the arrows. O (large balls) and Al (small balls).

to completely unravel the surface structure of this insulating oxide.

In the α-Al_2O_3 crystal structure, the O atoms are arranged in a hexagonal close-packed lattice with Al atoms occupying two out of three octahedrally coordinated interstitial sites in between stacked oxygen planes (figure 7). The (0001) surface terminates a R–Al–Al–O–Al–Al–O–R bulk stacking sequence, and three simple terminations obtained from truncating the crystal along the (0001) direction are normally considered (figure 7): (i) the oxygen-terminated O–R, (ii) the Al–O–R with Al in one of three possible octahedral sites and finally (iii) the Al-rich Al–Al–O–R–Al_2O_3 termination with Al in two octahedral sites. Energetically the Al–O–R–Al_2O_3 surface is always predicted to be the most stable, but theory coupled with thermodynamic modelling [103, 138] also predicts that the $Al_2O_3(0001)$ surface adopts a profoundly varying surface structure and composition when exposed to high temperature or to oxygen, hydrogen or water containing atmospheres. Previous experimental studies have shown that the surface of α-$Al_2O_3(0001)$ reconstructs structurally compared to the simple bulk-terminated (1 × 1) $Al_2O_3(0001)$ termination when it is exposed to high temperatures under reducing vacuum conditions [128–130, 142]. It was proposed that the alumina surface adopts this configuration due to gradual evaporation of oxygen from the topmost layer, and a 2.65 nm hexagonal superstructure, referred to as the $\sqrt{31} \times \sqrt{31}$R9° reconstruction, spontaneously evolves when the surface is heated above ∼1200 °C [131, 142]. The $\sqrt{31} \times \sqrt{31}$R9° surface reconstruction has been explained in terms of a coincidence pattern originating from the reorganization of an Al-rich overlayer resting on the bulk $Al_2O_3(0001)$ [143, 144], but the detailed atomic order of the structure remained unclear until the structure was imaged by NC-AFM. Barth and Reichling were the first to image the $\sqrt{31} \times \sqrt{31}$R9° structure in atomic detail with NC-AFM in 2001 [21], and later Wang *et al* provided further confirmation of the large-scale orientation of the $\sqrt{31} \times \sqrt{31}$ structure by using a so-called needle sensor AFM [44]. The structure that emerged from the NC-AFM images in [21] was consistent with the previous x-ray surface diffraction data describing the topmost surface layer as a hexagonally packed overlayer of Al atoms that completely wets the underlying Al_2O_3 substrate.

Lauritsen *et al* recently re-visited the surface in a study involving NC-AFM measurements with greatly improved resolution and, in an interplay with theoretical calculations, developed a detailed atomistic model for the $\sqrt{31} \times \sqrt{31}$R9° structure. Figure 8(a) shows a large-scale NC-AFM image of the $\sqrt{31} \times \sqrt{31}$R9° reconstruction after preparation under UHV, with the unit cell represented by a white rhombus. The atom-resolved NC-AFM image in figure 8(b) is taken from [45] and reveals that the $\sqrt{31} \times \sqrt{31}$R9° structure is rather well ordered, with a clear atomic structure with hexagonal symmetry and an interatomic distance of 3.01 Å. In line with previous studies [129, 131, 145], the emergence of the large $\sqrt{31} \times \sqrt{31}$ unit cell on the $Al_2O_3(0001)$ surface is explained by evaporation of oxygen from the topmost layer of Al_2O_3 when the crystal is exposed to a temperature around 1200 °C. The resulting excess of Al leads to the formation of a close-packed Al layer on top of the bulk-terminated Al_2O_3 surface, which wets the surface and is arranged on

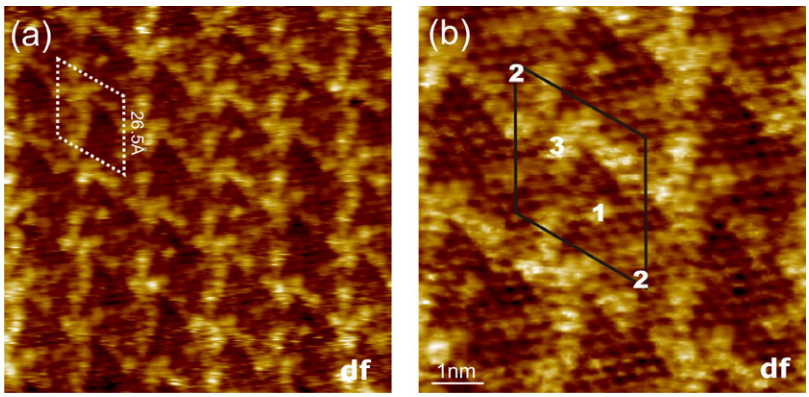

Figure 8. Atomically resolved NC-AFM images of the $\sqrt{31} \times \sqrt{31}$R9°-$Al_2O_3$(0001) surface (a) constant height (df) NC-AFM image (90×90 Å^2). Imaging parameters: $\Delta f_{set} = -20$ Hz, $A_{p-p} = 20$ nm. $f_0 = 330$ kHz, $k = 44$ N m^{-1}. The dark/bright contrast reflects a Δf range of ± 12 Hz. The white rhombus indicates the unit cell. (b) Constant height atom-resolved NC-AFM image (40×40 Å^2). Numbers indicate different stacking domains with the unit cell. Image parameters: $\Delta f_{set} = -24$ Hz, Δf-contrast: ± 13 Hz. Adapted with permission from [45]. Copyright 2009, American Physical Society.

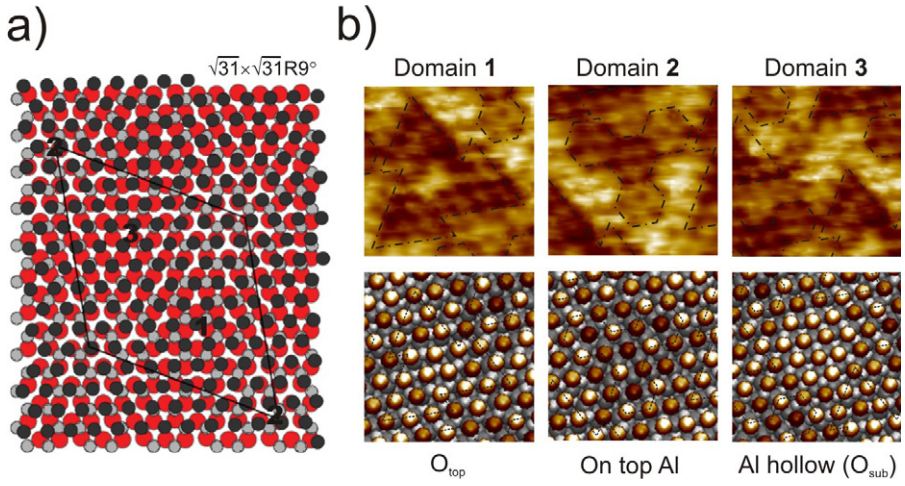

Figure 9. (a) Schematic illustration of a hexagonal Al layer with the lattice parameter (3.01 Å) placed on the Al_2O_3 substrate (Al–Al–O–R termination) and rotated by 32° to yield the periodicity of the $\sqrt{31} \times \sqrt{31}$R9° reconstruction. Three stacking domains indicated by the numbers 1–3 are present. Overlayer Al: small balls (dark grey). Substrate Al: small balls (light grey). Substrate O: large balls. (b) Upper part: zoom-in NC-AFM images of the three types of stacking domains contained in the $\sqrt{31} \times \sqrt{31}$R9° structure. Lower part: ball model of the corresponding stacking domains derived from figure 8(b). The colour scale is adapted to show relaxations with a brown–white colour scale, where dark reflects the largest inward relaxation. Adapted with permission from [45]. Copyright 2009, American Physical Society.

the surface in a non-epitaxial manner. The detailed structure of the $\sqrt{31} \times \sqrt{31}$R9° reconstruction seen in figure 8(b) was explained in terms of the misfit pattern arising from the lattice mismatch of the hexagonally arranged Al overlayer ($a_o = 3.01$ Å) relative to the Al_2O_3 substrate ($a_s = 4.75$ Å). The detailed epitaxial relationship was determined to be $[1\bar{1}0]$Al(111)/(R32°)$[11\bar{2}0]Al_2O_3$. In a simple model, the appearance of the $\sqrt{31} \times \sqrt{31}$R9° reconstruction seen in NC-AFM was then explained by the formation of a classic moiré structure reflecting the variation in stacking of the overlayer relative to the substrate. This configuration is illustrated in the ball model in figure 9(a), where a fixed hexagonally packed overlayer with the experimentally observed lattice distance of 3.01 Å is placed with the above-mentioned epitaxial rotation on a bulk-terminated Al_2O_3(0001) substrate, which results in a commensurate structure with the correct $\sqrt{31} \times \sqrt{31}$R9° periodicity.

The atom-resolved NC-AFM image in figure 8(b) also shows a very pronounced and systematic internal atomic structure inside each unit cell. This structure simply emerges from the periodic variation of the stacking in the different domains within the unit cell, as illustrated in figure 9(a). This is analogous to the variations seen in moiré patterns on fcc(111) metals, where overlayer atoms gradually shift between fcc and hcp stacking sites, except for the fact that the substrate is more complicated here. Indeed in the NC-AFM image, three different domains can be identified, which is consistent with the fact that an atom in the Al overlayer can principally adopt three different sites on a regular (0001) surface of Al_2O_3(0001). The different sites are illustrated in the ball model of figure 7 for a 1×1 unit cell of Al_2O_3(0001). The Al atoms can occupy a group of sites defined either by the on-top site on Al in the normal lattice sites of Al_2O_3, on-top O atoms of the uppermost O lattice, or in the hollow sites

in between Al and O. When the Al overlayer is placed on the substrate, this gives rise to three different stacking domains, as indicated by the numbers 1–3 in figure 9(a). DFT calculations have determined that, of the three different planes indicated in figure 7, an Al–Al–O–R substrate is the most stable in the presence of an Al overlayer, since the O–R and Al–O–R surfaces react with excess Al and form the same structure. In the Al–Al–O–R structure, 2/3 of the normal Al sites are already occupied by an Al atom, and one Al site is left vacant. The detailed variation in the contrast in the NC-AFM image (figure 8(b)) was explained by the buckling that appears from Al atoms that are placed on or near different sites on the substrate. A detailed comparison of the three different domains is illustrated in figure 9(b), where the upper panel are zoom-in images of the different domains, and the lower panel reflects a direct simulation of the relaxation perpendicular to the surface, indicated by a dark-to-bright colour scale. Here it is noted that the structure of the Al–Al–O–R substrate is clearly revealed in domain 2, where a feature consisting of four hexagon features arranged in a Y-shape appears for stacking on the Al sites. This was also reproduced in the simulation and was explained by the fact that the middle Al atom in the hexagons is allowed to relax by almost 0.3 Å into the surface, since it is placed on the 1/3 vacant sites of the Al–Al–O–R surface.

The study by Barth and Reichling, and later by Jensen *et al* [21, 146], also revealed the remarkable existence of a periodically modulated affinity for water adsorption which correlated with the periodicity of the $\sqrt{31} \times \sqrt{31}$ unit cell. Further NC-AFM experiments indicated that a reaction with water dosed to the vacuum led to the preferential formation of aluminium hydroxide or aluminium oxyhydroxide clusters at these domain boundaries [146, 147]. This observation was originally attributed to lower coordinated atoms at the disordered domain boundaries of the previous model for the $\sqrt{31} \times \sqrt{31}$ unit cell [21], but in light of the well-ordered atomic model proposed from the NC-AFM studies in figure 9(a), the observation of a periodically modulated affinity seems rather induced by the different chemical environment of differently stacked Al atoms contained within the unit cell, or alternatively from variations in the strain field of the substrate.

Alumina can form surfaces with a stunning variety of structures and reconstructions. Recently, three structures that greatly differ from what is known from the bulk have been observed by NC-AFM and STM on alumina thin film systems grown on metal surfaces, and two of them have been explained by theoretical simulations [13, 14, 48]. It is, however, not a coincidence that NC-AFM studies on bulk insulating alumina have so far only been able to address the high-temperature phases of $Al_2O_3(0001)$, and many further studies remain to be done for Al_2O_3 surfaces. The requirement for very clean, flat surfaces for high-resolution NC-AFM necessitates very high temperatures during surface preparation, and once the $\sqrt{31} \times \sqrt{31}$ structure is formed, it is surprisingly resistant toward re-oxidation under normal UHV conditions. Already some of the first studies on the system have reported on an unusual stability of the $\sqrt{31} \times \sqrt{31}$ reconstruction [129], and later studies have shown that the structure remains stable during annealing in oxygen up to 10^{-5} mbar [44], and it even seems to remain stable during transfer under ambient (water free) conditions [131]. LEED studies have reported on other surface structures present at lower temperature [130, 132], but these have not been resolved by AFM so far. In order to access a wider range of the surface phase diagram it seems necessary to develop more sophisticated preparation schemes for $Al_2O_3(0001)$ surfaces. In this regard, it is noteworthy that recent contact-mode AFM images recorded in liquid water have revealed a (1×1) terminated $Al_2O_3(0001)$ [148], but since contact-mode AFM does not resolve single adsorbates or defects it was unclear from these studies whether the surface was plain O-terminated or terminated by OH groups.

5. Polar ZnO(0001) surfaces

The interest in zincoxide (also called zincite, ZnO), and in particular the surfaces of ZnO, has increased tremendously in recent years. ZnO is a wide band-gap metal oxide with a unique combination of tunable semiconducting and transparent optical properties, and it has a very wide range of applications in areas such as optoelectronics, photovoltaics, light emitting devices, catalysis and gas sensors [5]. In addition, the substantial progress made in nanofabrication methods has led to the synthesis of a multitude of tailored ZnO nanostructures and surfaces with interesting and unique functional properties [6, 7, 149]. The fundamental atomic-scale structure of ZnO surfaces has been the focus of a very intense scientific debate. Much of the debate stems from the fact that the low-index (0001)-type ZnO surface termination is an example of a *polar* surface. Polar surfaces are exposed when there is a finite dipole moment in the repeat unit cell of the bulk perpendicular to the surface [150, 151]. This is the case for a large group of solid ionic compounds, including a wealth of metal oxides, built by stacking differently charged atomic layers. Polar surfaces formed by a simple truncation of the crystal lattice are, however, unstable due to their diverging electrostatic energy, and the surface must therefore be energetically compensated by adopting a modified or reconstructed surface structure. When the wurtzite ZnO crystal (figure 10(a)) is sliced perpendicular to the (0001)-axis, two principally different polar surfaces are formed. These surfaces are both exposed in natural crystals, namely the Zn-terminated ZnO(0001) and the O-terminated ZnO($000\bar{1}$) surface. Electrostatic considerations [151, 152] predict that the removal of a quarter of the surface ions (O^{2-} for ZnO($000\bar{1}$) and Zn^{2+} for ZnO(0001)) will compensate the resulting dipole and result in stable non-polar surfaces of this type. However, despite intense efforts, no such general reconstructions have been observed for either of the (0001)-type ZnO surfaces (see e.g. [153–161]), and the fundamental mechanism for stabilization of the polar surfaces therefore remains an open issue. A very important missing piece of information concerns a detailed microscopic (local scale) characterization, since this has not been revealed by traditional surface structure determination tools such as low-energy-electron diffraction (LEED), ion scattering and surface x-ray diffraction (SXRD). This is important, since defects, such as step edges, holes and islands on the surfaces, seem to play a major role in the

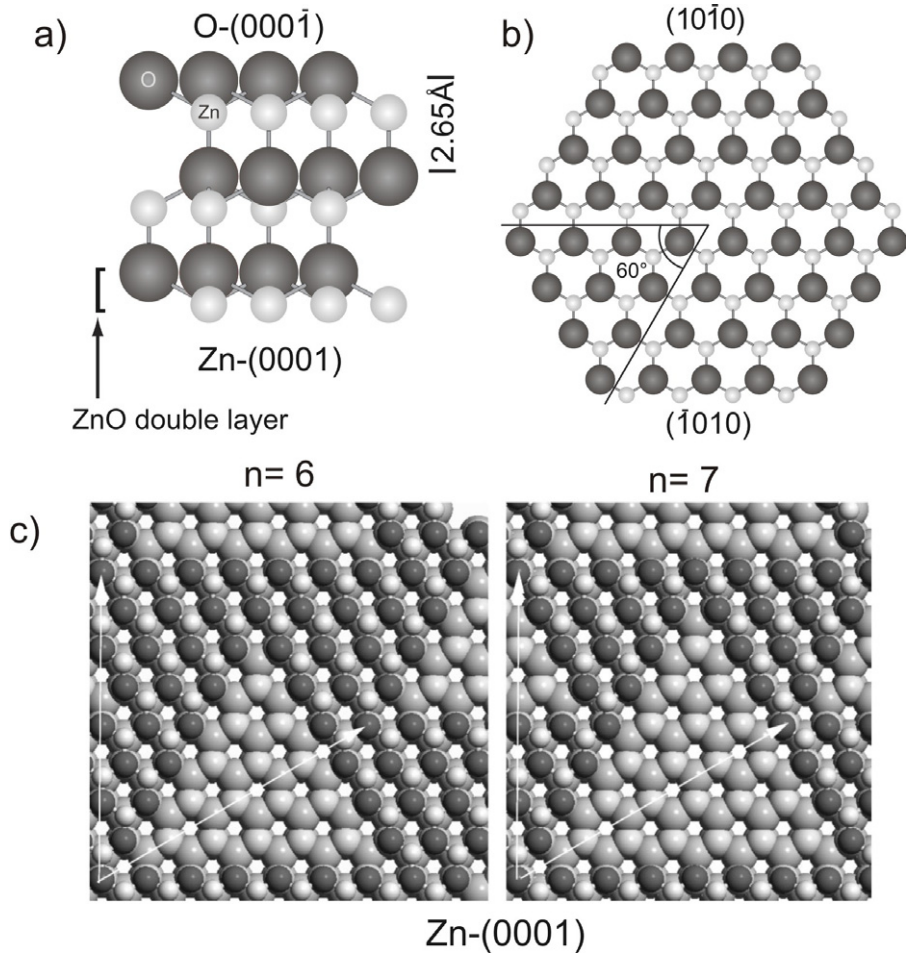

Figure 10. (a) ZnO crystallizes in the wurtzite structure and is built up of alternating hexagonal planes of four-fold coordinated Zn and O atoms, forming ZnO double layers. The ball model is a side view illustrating a hypothetical structure terminated by ideal Zn-terminated (0001) surface and O-terminated (000$\bar{1}$) surfaces (b) ball model illustrating the top layer of the O-terminated (000$\bar{1}$) sheet and the two types of edges terminating such a layer. (c) The two ball models (top view) are adapted from [104] with permission (G Kresse *et al*) and show two variations of the most stable defect structure on the Zn-terminated (0001) surface consisting of triangular, one layer deep pits of varying size. The triangular pits are terminated by O-rich {10$\bar{1}$0} edges.

compensation mechanism, and these defects do not typically appear in well-defined periodic patterns and are therefore undetectable with the averaging techniques mentioned above. In addition, the ZnO surface is highly sensitive, in particular to water and hydrogen, during preparation, and as discussed, e.g. in a recent review on ZnO surfaces [153], it is likely that some differences reported for the same surfaces in the literature are related to variations in preparation methods and specific conditions of the experiment. Here, again, NC-AFM emerges as a powerful technique that can solve the structure of the surface and analyse the structural properties of the surface at the atomic scale. STM has already played an important role in discovering a mechanism to stabilize the Zn-terminated (0001) surface of ZnO. The Zn-terminated surface was conducting enough to perform stable STM imaging, and in combination with density functional theory (DFT) it was revealed that the stabilization under ultra-high vacuum (UHV) conditions is preferentially caused by the spontaneous formation of a high concentration of Zn-deficient triangular pits (see figure 10(c)) terminated by under-coordinated O atoms with otherwise bulk Zn-terminated ZnO(0001) terraces [104, 162]. The accumulated surplus of O associated with the number of edge sites of the defects was compatible with the stabilization criterion that the surface should contain about 25% less Zn atoms than O atoms. In addition, the proposed model in figure 10(b) furthermore explained the previous observation of a non-reconstructed (1 × 1) pattern from LEED, which reflects the atomic structure on the extended terraces between the pits.

An atomic (1 × 1) pattern on the surface was, however, never successfully resolved by STM, and some controversy still remains concerning the surface structure, as discussed in recent reports on different reconstructions [163, 164] and effects of temperature [158]. The apparent difficulties in achieving atomic resolution by STM may be related to the rather low conductivity of ZnO. AFM, on the other hand, is not hampered by low conductivity and, therefore, seems to be a more suitable technique for the imaging of the atomic structure of ZnO surfaces. So far, however, only few NC-AFM studies have been published on ZnO. In a recent paper, Torbrügge *et al* presented real atomic resolution on the Zn-terminated ZnO(0001) surface using NC-AFM.

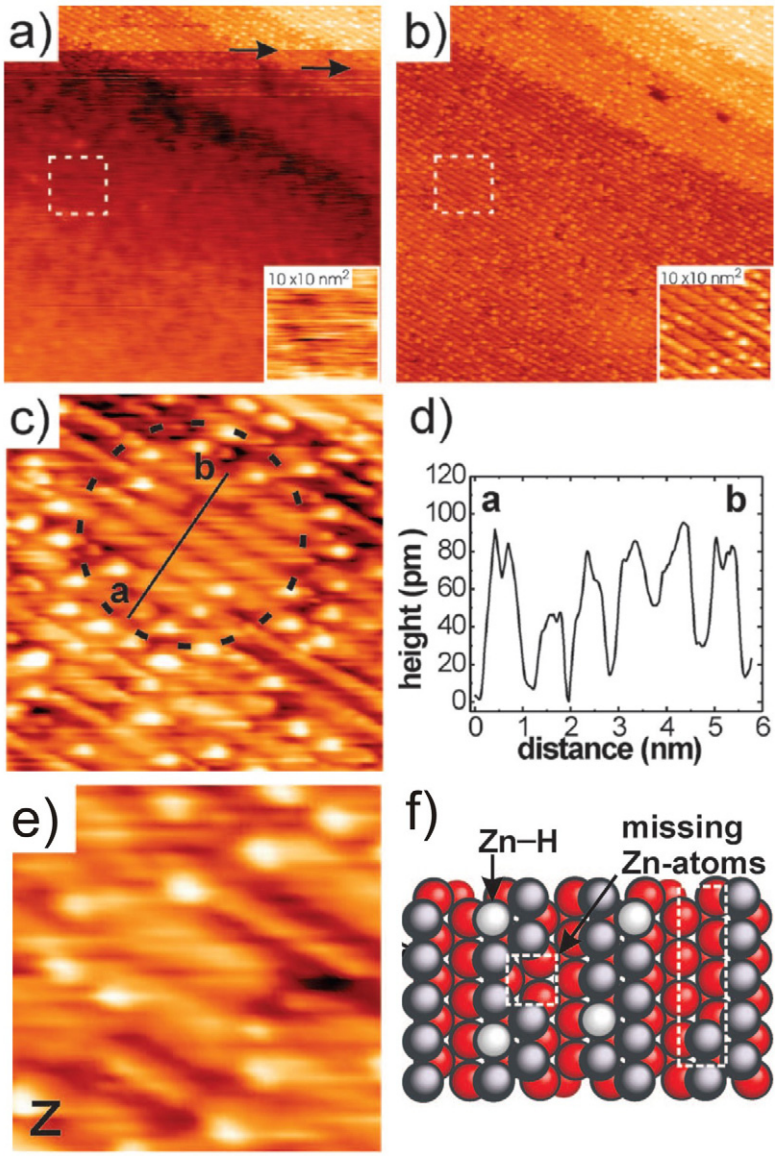

Figure 11. (a) and (b) Two consecutive topographic NC-AFM images of the Zn-terminated ZnO surface prepared under UHV conditions by annealing to 1150 K. The arrows indicate the points at which a contrast change is observed, and atomic resolution is obtained (c) atom-resolved NC-AFM image showing a zoom-in on the flat terraces. The striped structure reflects a (1 × 3) reconstruction of the surface (d) line scan across the row structure as indicated in (c). (e) Atom-resolved NC-AFM image showing the presence of two types of defects associated with Zn–H groups and missing Zn atoms. (f) Ball model of the (1 × 3) reconstruction with the observed defects. Adapted with permission from [53]. Copyright 2009, American Chemical Society.

The Zn-terminated Zn(0001) surface in [53] was prepared in such a way that it exposed more flat and extended terraces compared to those previously observed by STM [154] and AFM [52] studies, and in some parts of the surface it exhibited a rather low concentration of stabilizing triangular pits, such as those in figure 10(b). On the completely flat areas, which were estimated to cover about 10% of the surface, however, a (1 × 3) reconstruction of the surface could be observed in atom-resolved AFM images, as shown in figure 11(b). The atomic resolution in NC-AFM was found to be strongly tip dependent, as exemplified by two consecutive NC-AFM images of the same surface region in figures 11(a) and (b). Here the scanning motion was performed from the bottom upwards, and it is observed in the top of the frame in figure 11(a) that the NC-AFM contrast suddenly changes from a blurry non-periodic pattern into a sharp (1 × 3) pattern. As in the case of TiO_2 (figure 6) [27], the shift in NC-AFM contrast may be related to an atomic level change in the chemical forces probed with the nanoapex of the AFM tip. In this particular case, a likely scenario is that the tip picked up an O atom as it passed over the step edge in the top of the frame (figure 11(a)). Figure 11(c) reveals the NC-AFM atomic contrast of the (1 × 3) pattern in higher magnification, and the line scans in figure 11(d) were used to confirm the dimension of the (1 × 3) of unit cell. The detailed contrast seen in NC-AFM was compatible with a double row structure imaged with a bright contrast interrupted by a missing row, and the structure of the (1 × 3) surface was

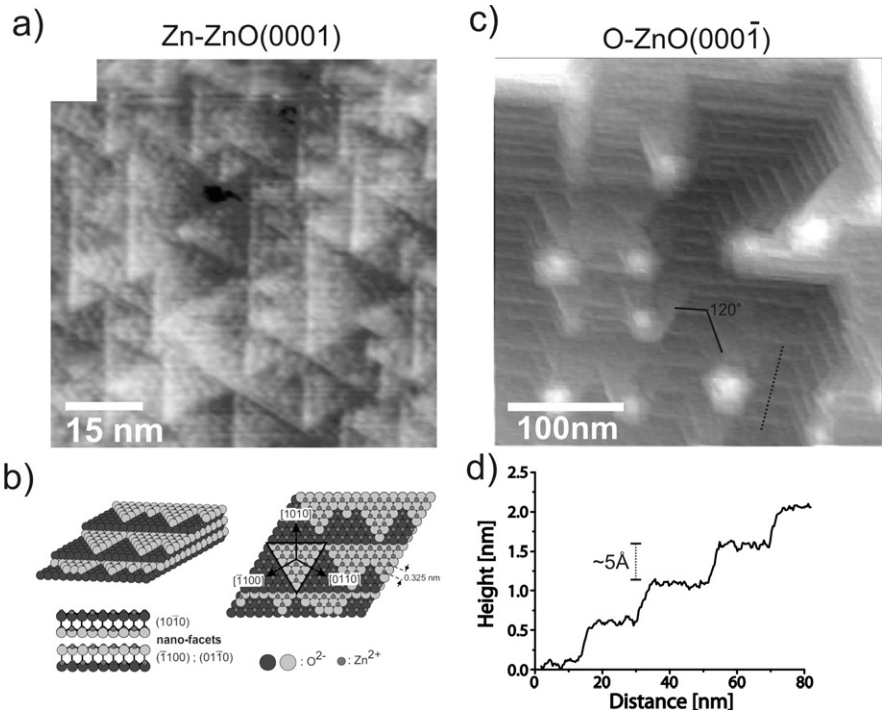

Figure 12. (a) Large-scale image of facetted Zn-terminated ZnO(0001), exposing a triangular morphology terminated by O-rich edges. (b) Ball models of the facetted Zn-terminated ZnO(0001) surface. (a) and (b) are reproduced from [52] with permission. (c) Large-scale NC-AFM image of the O-terminated ZnO(0001) surface, exposing a hexagonal morphology [54]. (d) Line scan across several step edges in (c).

therefore explained by a missing row structure in which every third row of Zn atoms were removed, as shown in the ball model in figure 11(f). Two types of defects were also observed on the row structure in the NC-AFM images. As shown in figure 11(e), one type showed up as protrusion located on the Zn rows, and was attributed to H atoms adsorbed on Zn to form a Zn–H group. Additionally, in some parts of the images the double strand of Zn atoms would be reduced to a single strand, which indicated the presence of single or multiple Zn vacancies, as illustrated in the ball model in figure 11(f). In principle, the (1 × 3) reconstruction overcompensates the dipole of the Zn-terminated (0001) surface, since it is formed by removal of ∼33% of the Zn atoms. However, as pointed out by Torbrügge *et al*, the (1 × 3) structure exists in rather small domains and it may be that the 33% overcompensation is balanced on the larger scale by other effects related to the co-existing triangular domains which dominate the surface in most other regions. The main conclusion was therefore that several structures co-exist on the Zn-terminated surface which then participate in the stabilization of the surface on an equal level. This is corroborated by another NC-AFM study by Ostendorf *et al* [52], who investigated the role of a high concentration of steps on the surface. The NC-AFM images from [52] shows a facetted surface morphology with triangular saw tooth structures on the small terraces. This surface morphology co-exists with the flatter areas discussed above and does not exhibit the triangular pits nor the (1 × 3) reconstruction, but instead adopts the saw tooth facet structure in order to optimize the amount of the same edges that terminate the triangular pits in figure 10(c), i.e. oxygen-terminated edges of the {10$\bar{1}$0} family (see figure 10(c)). The opposite {$\bar{1}$010} edges in figure 10(c) are Zn-terminated and are therefore avoided in the facet structure by adopting the characteristic edge structure. The model of the step edge structure on the Zn-terminated (0001) surface is visualized in the ball models in figure 12(b).

The O-terminated ZnO(000$\bar{1}$) surface (figure 10(a)) has been examined to a much lesser extent. Again electrostatic considerations predict that the removal of about 25% of the surface oxygen would stabilize the surface, but so far diffraction studies report a non-compensated (1 × 1) surface structure, which could indicate, in analogy with the mechanism for the Zn-terminated surface, that the detailed surface morphology is very important. H adatoms on the O-terminated surface have been proposed to plays a major role, but stabilization by H does not seem to be compatible with a (1 × 1) structure [155, 156]. Interestingly, a similar (1 × 3) missing row O structure has also been reported on the O-terminated ZnO surface by LEED and He atom scattering studies [153, 165], but microscopy evidence of and calculations for this structure have not been produced so far. STM images showing the large-scale morphology of the surface have been published [154], but it has also been reported that the surface becomes insulating in the clean state after several preparation cycles [154]. Given the recent debate in the literature [153, 159, 166], the atomic-scale surface structure of the O-ZnO(000$\bar{1}$) surface and the mechanism for its stabilization must still be considered as a very open issue. It is, however, clear that the O-terminated surface is structurally and chemically different from the Zn-terminated one. In practice, the two facets can be discerned from their etching behaviour, but the differences are also visible on the

microscopic level in NC-AFM images. Figure 12(c) shows a NC-AFM topographic image of the O-terminated surface, imaged after more than 20 sputtering cycles, where the ZnO substrate has reached a totally insulating state [167, 54]. The UHV prepared O-terminated ZnO(000$\bar{1}$) surface also exhibits areas with a high concentration of step edges, similar to the Zn-terminated surface, but in contrast to the saw tooth morphology (figure 12(a)), the stepped regions of the O-terminated ZnO surface adopt a hexagonal morphology reflecting 120° bends between terraces. At first sight this structure is incompatible with the general notion that Zn-terminated {$\bar{1}$010} edges should be preferred for the O-terminated surface, which would require the same 60° bends. However, a measurement of the step height reveals that all steps are double steps (0.52 nm) and thus consist of a full unit cell (figure 10(a)). The double height step edges therefore reflect O-terminated edges stacked on Zn-terminated edges, or vice versa. Effectively this implies that the effect of placing excess Zn atoms on the edges is annulled for this surface geometry, and tentatively assuming that the edge structure of the {$\bar{1}$010} and {10$\bar{1}$0} edges is unperturbed, therefore, the step edges do not seem to participate in the overall compensation of the surface dipole of the O surface.

In conclusion, the recent microscopic insight based on NC-AFM shows that the surface structure of ZnO(0001) surfaces is very sensitive to large-scale morphology effects and the exact conditions under which the surface was formed. Further NC-AFM studies aimed at resolving the atomic-scale surface structure, especially of the O-terminated surface, could provide the key insight needed to resolve the mechanism for stabilization of both surfaces.

6. CeO_2(111)

Materials based on ceriumdioxide (also called ceria, CeO_2) are important in diverse industrial and research areas, such as solid-fuel cell technology and catalysis, both intimately related to the production of hydrogen [168, 169]. In this context, ceria is discussed as a support for catalytically active noble metal particles promoting noble metal or metal ion catalytic activity and as an oxygen buffer absorbing oxygen into the solid phase for transport to the catalytically active site [170–174]. A premier application for ceria based catalysis exploiting this transport mechanism is the 3-way catalytic converter commonly used in motor vehicle exhaust systems [175, 176]. The capability for storing and releasing oxygen is believed to be due to the rapid formation and elimination of oxygen vacancy defects at the ceria surface, however, a final confirmation of this notion is still lacking but is the motivation of studies aimed at directly observing surface chemical processes on ceria surfaces at the atomic scale. Due to its widespread use and importance in catalysis, ceria materials have already been subject to numerous studies to explore the catalytic activity for specific reactions and the tailoring of ceria materials [177–181]. The most widely studied reaction is the so-called water gas shift reaction, providing an efficient way of hydrogen production [172, 182–187]. Motivated by studies on the optimization of ceria catalytic materials [188] for this and related reactions, the geometric and electronic structure of ceria nanoparticles and ceria model surfaces, their reactivity, defects and metal particles deposited [189–191], have been investigated by electron microscopy, diffraction and spectroscopic methods. There is also a large number of theoretical studies simulating the bare surface, [192–197] vacancy defects [198, 199], deposited metal atoms and particles [200–202] and surface reactions [203, 204]. For a direct observation of the surface and surface processes at the atomic scale, defects and adsorbates at slightly and strongly reduced CeO_2(111), the thermodynamically most stable [192] and easily prepared crystallographic termination of ceria, have already been studied by STM [205, 206] and NC-AFM [56, 64].

Although it is possible to explore ceria surfaces using STM at elevated temperatures by working at the very limit of this technique, NC-AFM arises as the natural method for the room-temperature and low-temperature characterization of atomic defects and adsorbates at the surfaces of this wide band-gap (6 eV band-gap) oxide. To achieve a spatial resolution revealing all atomic details, however, as demonstrated below, requires an instrument with the highest sensitivity, such as a commercial force microscope optimized for the purpose [207]. The surface preparation of CeO_2(111), based on *ex situ* mechanical polishing and sputter/anneal cycles in UHV, is straightforward and, by a variation of the preparation details, it is possible to create a surface with large atomically flat terraces that are relatively free of defects, except regular step edges [58, 208] or a surface with a high density of vacancies and other defects, some of them not yet unambiguously identified [60]. Well identified features on the surface are water molecules, which are found to adsorb readily on CeO_2(111) spontaneously from the ambient atmosphere (residual gas or water dosage) or by transfer from the scanning AFM tip [59].

The typical appearance and morphology of a defect free CeO_2(111) surface is shown in figure 13(a). Large atomically flat terraces are separated by steps with a height of 0.31 nm, corresponding to one O–Ce–O triple layer (figure 13(b)). The atomic resolution detail image from figure 13(c) shows the (1 × 1) termination of the surface, as highlighted by the model in figure 13(d). In previous work, it has been demonstrated that in NC-AFM studies on CeO_2(111), most likely the topmost layer of the oxygen-terminated surface is imaged [62], although, a final proof by an image calculation is still missing. The edges of the regular step structures in figure 13(a) enclose an angle of 120°, resulting in the formation of a characteristic surface morphology exhibiting hexagonally shaped pits (figures 13(a)i and 13(a)ii) and islands, whereas hexagonal pits again exhibit a depth corresponding to a triple layer (figure 13(e)). This is a general morphology for (111) orientated CeO_2 surfaces that has been found in thousands of measurements on surfaces prepared under conditions of thermal equilibrium. The hexagonal shape of the pits reflects the hexagonal symmetry of the surface, which can be traced down to the atomic scale with NC-AFM by imaging the atomic structure of straight step edges bordering the pit. This allows conclusions to be drawn on the energetic conditions of certain step structures of this surface [208]. Another feature commonly found on CeO_2(111) is the presence of screw

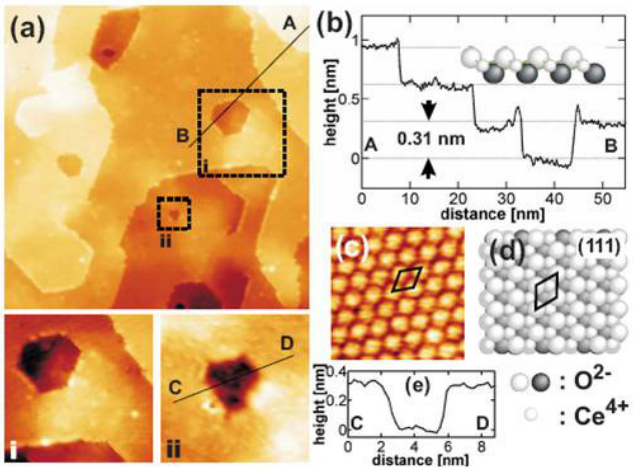

Figure 13. (a) Topographic NC-AFM images of the $CeO_2(111)$ surface morphology observed directly after preparation (image size 100×100 nm^2). (b) Height profile taken along the straight line indicated in (a) revealing steps of triple layer height. (c) Atomically resolved image (image size 2.3×2.3 nm^2) together with a schematic model (d) of the stoichiometric oxygen-terminated (111) surface. (e) Height profile as indicated in (a)ii. Reproduced with permission from [208]. Copyright 2008, American Institute of Physics.

dislocations, which are most obvious as step edges emerging in the middle of a terrace. Several of them are present in the image from figure 13(a), demonstrating that the presence of such screw dislocations allows a smooth transition between terraces on different levels which might be relevant for surface diffusion processes.

Among the multitude of atomic-scale structural irregularities that can be observed on $CeO_2(111)$, vacancies are an important, and presently the best understood, class of defects. Figure 14 explains the typical topography ascribed to a surface and a subsurface oxygen vacancy, as outlined in [61]. In such images, the surface oxygen vacancy (figures 14(a) and (c)) can be recognized as a missing atom surrounded by six atoms that protrude about 12 pm (see figure 14(b)) from the unperturbed layer of oxygen atoms in which the surface is terminated. This height difference agrees well with the vertical displacement predicted by first-principles calculations for the six oxygen atoms next to a surface vacancy [194]. The results from these calculations also predict a slight lateral relaxation of the atoms surrounding the vacancy that tends to form pair-like structures (see model in figure 14(d)), an effect observed in NC-AFM images as well (see figures 14(a) and (c)). According to this theoretical calculation, the two excess electrons left from the missing surface oxygen ion localize at two of the three Ce^{4+} ions of the second layer next to the vacancy, reducing them to Ce^{3+} ions [194]. Such charge localization would imply an asymmetry in the appearance of the vacancy that has so far not been observed experimentally, which may point to a charge localization further away from the vacancy, as was proposed in a later theoretical study [209].

The appearance of the subsurface oxygen vacancy (figures 14(e) and (g)) is as three oxygen atoms protruding approximately 20 pm from the surface (see figure 14(f)) and spaced by two lattice constants, while the three inner oxygen atoms separated by one lattice constant are slightly relaxed towards the bulk (see model in figure 14(h)). With NC-AFM imaging, it has been possible to identify the subsurface oxygen vacancies, because of the excellent agreement of the observed topographic features with predictions from first-principles calculations for the surface structure and relaxations, and also by a characteristic pattern in the NC-AFM dissipation signal discussed below [61]. In the case of the subsurface oxygen vacancy, calculations predict that the two excess electrons are also localized at two Ce^{3+} ions of the second surface layer next to the defect [194]. This charge localization implies a local symmetry breaking that might play a role in the ordering of these defects observed at high concentrations [61]. It is still under discussion whether the structure associated with a surface oxygen vacancy is energetically more favourable than the one ascribed to a subsurface oxygen vacancy [192, 194]. While STM experiments performed at elevated sample temperatures suggest that both defects are equally distributed [205], the NC-AFM evidence collected at room temperature points to a variability in the distribution of surface and subsurface oxygen vacancies from terrace to terrace over the same surface, with regions where almost no subsurface oxygen vacancies are found and other surface areas where a high concentration of them can be clearly observed. It is found that on terraces dominated by subsurface oxygen vacancies, the large amount of protruding oxygen atoms makes it difficult to identify the subsurface oxygen vacancies upon a first inspection [61]. However, NC-AFM imaging allows for unambiguously locating the exact position of the subsurface oxygen vacancies by an analysis of the dissipation signal recorded simultaneously with topography. This signal is related to the amount of energy lost by the cantilever due to nonconservative interactions with the individual surface atoms [210, 211]. A comparison between topography and dissipation signals over the same surface area, reveals that each group of three protrusions apparent on the dissipation image exactly matches with the lattice positions of the three inner surface oxygen atoms just above the subsurface oxygen vacancy. In a dense array of subsurface vacancies, this allows a clear discrimination of vacancy sites from those where a vacancy is pretended by protrusions from surrounding vacancies [61].

This means of identification is important as, on terraces with a high concentration, clustering of subsurface vacancies into regular arrays is observed. However, it is found that these defects do not condense into a close-packed layer, but appear in ordered arrays with a tendency to form linear patterns, leaving defect free areas in between. Such arrays might be the consequence of a delicate balance between attractive and repulsive interactions among subsurface oxygen vacancy structures, and it has been speculated whether interactions involving the Ce^{3+} localized charges are part of this balance [61].

Ceria has already proven itself as an oxide material, not only demanding NC-AFM imaging if one is interested in high-resolution surface studies, but also being of good nature for such investigations. On the (111) surface, excellent atomic

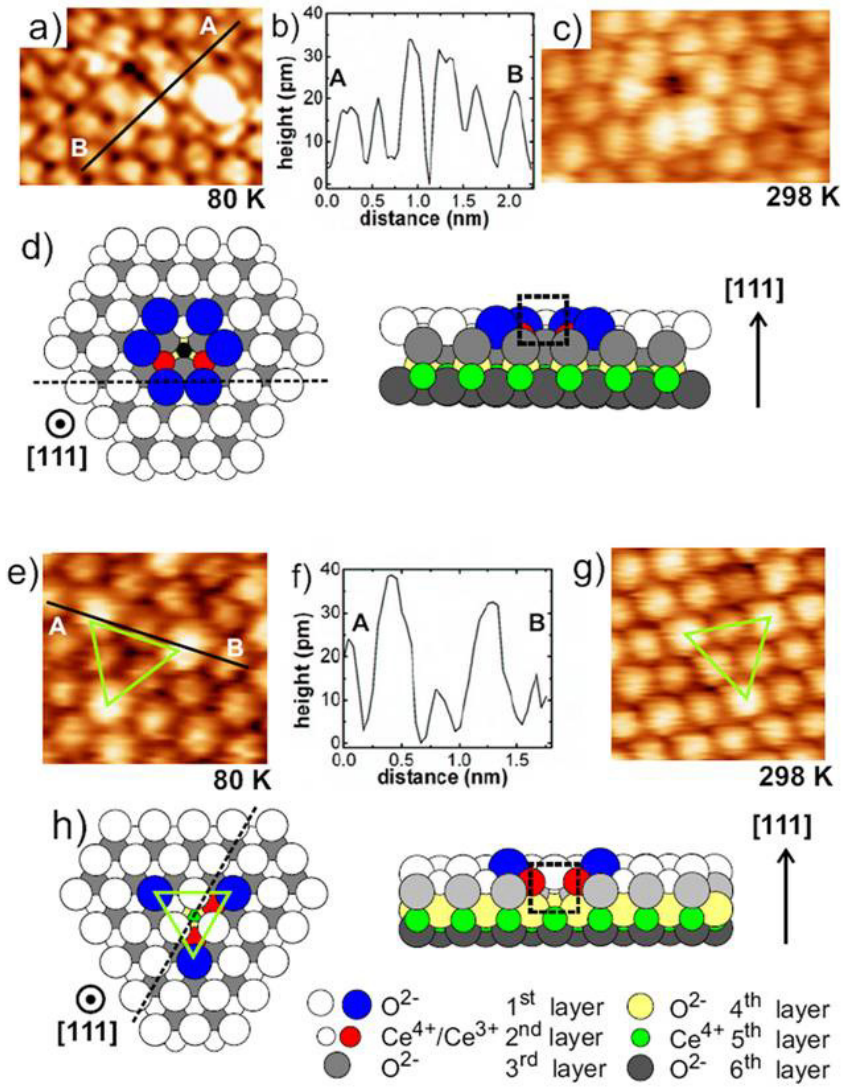

Figure 14. NC-AFM topographic images of a surface ((a) and (c)) and a subsurface ((e) and (g)) oxygen vacancy, recorded at 80 K and room temperature. (b) and (f) show height profiles as indicated by the solid lines in (a) and (e). Structural models (d) and (h), for both types of oxygen vacancies, are shown in top view and profile view along the dashed lines in the top view panels, respectively. Adapted from [61].

contrast revealing subtle structural details of surface defects is routinely obtained and the apparent atomic structure is often found to be in stunning agreement with the atomic topography predicted by model calculations. The wealth of interesting experimental findings already available from NC-AFM investigations has so far, however, raised more questions than it has answered, and the potential of NC-AFM imaging on this oxide is far from being exhausted. In addition, many experimental findings still await a conclusive theoretical description. Among the many interesting issues to be settled, where NC-AFM imaging and spectroscopy can be anticipated to provide contributions, are a full description of hydrogen defects and the question of charge localization at isolated surface Ce^{3+} centres, unravelling details of water adsorption and manipulation at the surface, describing the nucleation, growth and sintering of metallic particles on the surface and, finally, directly observing surface chemistry to unravel catalytic processes at the atomic level.

7. Perspectives on future NC-AFM research on metal oxide surfaces

The NC-AFM technique has developed tremendously during the last decade, and matured from being a promising technique under development to a versatile tool for atomic resolution analysis in the study of complex nanoscale systems. In particular, its ability to probe atomic-scale structures on insulating surfaces makes it a very attractive technique for oxide studies and in many other fields. This does not only apply to the study of bare oxide surfaces, but even more to systems involving more complicated nanostructures, single molecules, molecular assemblies, self-assembled monolayers, quantum dots or nanoclusters that are decoupled from a conducting bulk material. Below we highlight some of the most promising future directions of NC-AFM in the context of research on metal oxide surfaces.

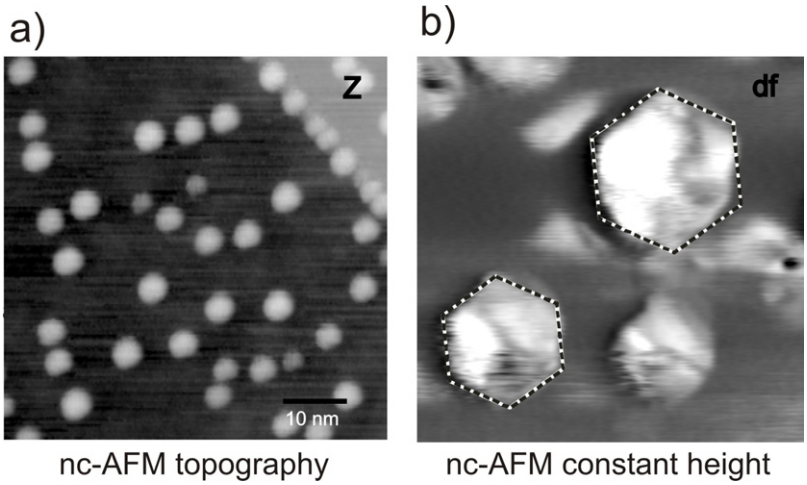

Figure 15. Clusters supported on $Al_2O_3(0001)$. (a) Topographic NC-AFM image of ∼3–4 nm wide Cu nanoclusters grown after deposition of 0.25 ML Cu and annealing to 300 °C. (b) Zoom-in image on a few nanoclusters revealing a clear hexagonal top facet of the two highest nanoclusters. The image was recorded in the constant height mode (Δf-mode). Adapted from [147] with permission. Copyright 2008, American Chemical Society.

Nanoparticles on metal oxides

The interest in studying nanoparticles supported by insulating metal oxides is strongly motivated by the use of such systems in heterogeneous catalysis. Heterogeneous catalysts are typically very complex structures consisting of nanoparticles of (transition)-metals, metal sulfides, or metal oxides supported on porous ceramic supports, such as Al_2O_3, TiO_2, CeO_2 or ZnO, or a mixture of such materials [212]. The main role of the metal oxide is to avoid coalescence of the nanoparticles and to secure bonding to a firm support, and in this way ensure a high surface area of the catalytically active nanoparticles. Many studies have, however, shown that the interaction with the support (and its defects) plays an active role in determining the detailed shape and structure, and hence the catalytic activity and long term stability of nanoclusters on the surface [213–215]. Moreover, the support may also interact synergistically with the active nanoparticles by atom or molecule exchange (spill-over) at the interface between the nanoparticle and the metal oxide [216]. In general such support effects are poorly understood at the atomic level, and there is a need to achieve a much better fundamental atomic-scale understanding of the detailed morphology of catalytically active nanoclusters and their interaction with the oxide. In this context, NC-AFM is an indispensable tool for addressing these issues for the insulating group of metal oxides. The typical approach is to choose an appropriate model catalyst, characterize the state of the metal oxide surface, its defects and prevalent adsorbates, and in a second step determine the morphology and stability of the deposited metal nanoclusters and how they are influenced. A similar 'model catalysis' strategy has successfully been used for STM studies of a wide range of conducting systems (see e.g. [12, 217–222]) to provide a detailed insight into the morphology of supported catalytically active nanoparticles.

For studies of nanoparticles, the minute forces exerted on the particles in the non-contact mode of operation is a major advantage over other AFM techniques that may be used, since damage or tip-induced movement of particles is a major obstacle for nanoparticle studies. As for any scanning probe technique aimed at revealing topography, the lateral resolution in imaging of 3D objects is fundamentally limited by the sharpness of the tip. Generally, a 3D object is imaged with a broadened contour due to gradual interactions with the side of the AFM tip as it is scanned across the 3D object. This effect is referred to as *tip-broadening* and can lead to erroneous conclusions about the lateral dimension in some extreme cases, specifically for small nanoparticles. Nevertheless, AFM tips are now commercially available with a nominal tip diameter of about 2 nm, which has enabled a rather reliable characterization of the 3D dimensions of nanoclusters on surfaces in recent NC-AFM studies [28, 147, 223–228]. To some extent, the tip-broadening can be eliminated by applying the NC-AFM in a quasi-constant height mode, when the interest is focused on imaging the top facet contour of a flat particle, as first demonstrated for Pd nanoclusters grown on MgO [226, 229]. The same method was recently also used by Jensen *et al* to resolve the hexagonal (111) top facet of Cu nanoparticles supported on Al_2O_3, as shown in figure 15 [147]. Following the methodology previously developed for STM characterization of Pd and Cu nanoclusters [230–232], it was furthermore possible in [147] from the NC-AFM characterization of the Cu cluster dimension and the knowledge on the orientation of the cluster facet relative to the substrate to quantify the work of adhesion (W_{adh}) for Cu on clean and hydroxylated Al_2O_3 surfaces. The analysis showed that Cu wets more strongly hydroxylated surfaces, which is presumably due to the formation of Cu–O linkages to the Al_2O_3 support that do not exist for the vacuum-prepared clean surface.

Non-contact AFM in liquids and at elevated pressures

Many chemical, and virtually all biological, phenomena occur with the participation of a liquid phase and, driven by

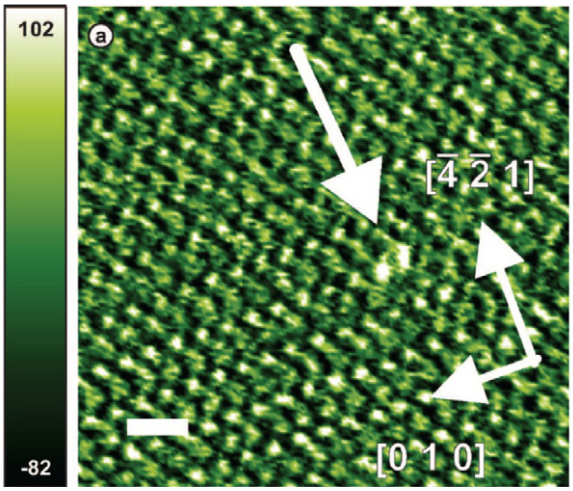

Figure 16. Atomically resolved NC-AFM image of $CaCO_3(10\bar{1}4)$ recorded at room temperature in water. The scale bar is 4 nm. The arrow indicates a surface defect. Reproduced with permission from [238]. Copyright 2009, American Chemical Society.

the interest in studies on polymers and biological systems, the originally purely UHV based NC-AFM technique is now conquering the ambient air and liquid condensed phase environments [233]. However, the presence of a gaseous ambient or a liquid dramatically reduces the quality factor (Q-factor) of the oscillating cantilever, significantly reducing measurement sensitivity. It has been shown recently, however, that this can be overcome by a radical optimization of the NC-AFM detection optical path, photodetection, pre-amplification and signal processing [234, 235]. With such developments, it has indeed been demonstrated that atomic resolution NC-AFM is achievable in liquids [236, 237]. In the context of metal oxide studies, Sasahara *et al* have also presented atom-resolved NC-AFM images of a $TiO_2(110)$ surface recorded in a dry atmospheric pressure N_2 environment [35]. Despite the reduction of the Q-factor due to the presence of the gas, it was still possible to resolve the characteristic row structure of the TiO_2 surface, and even resolve single atomic defects. As an example of the application of NC-AFM in a liquid for imaging a carbonate mineral, Rode *et al* demonstrated true atomic resolution on the $(10\bar{1}4)$ cleavage face of $CaCO_3$ (calcite) kept in a clean aqueous environment [238]. A representative result is shown in figure 16, where the details of the $CaCO_3(10\bar{1}4)$ unit cell are resolved as a zigzag row structure along the $[\bar{4}\bar{2}1]$ direction. Furthermore, an atom-sized defect could be resolved, as indicated by the large arrow in the figure. Interestingly in [238], complementary sets of atom-resolved images of $CaCO_3(10\bar{1}4)$, which could be interpreted as either the O or Ca ion lattices, were also presented. These two types of contrast modes were in analogy to the studies of TiO_2 performed under UHV (see discussion in section 3), and explained by different tip terminations (positively or negatively terminated tip). The apparent resemblance indicates that the same physical principles may apply to the short-range forces dominated by electrostatic interactions responsible for atomic resolution in NC-AFM performed under liquid conditions as in the UHV, despite the presumably large influence of the surrounding liquid phase.

The recent successful reports of NC-AFM in liquid and at elevated pressures thus illustrates that atomic resolution is not fundamentally limited by the liquid and gas environments. The technical improvement and development of new probes operated at low oscillation amplitudes may lead to further developments in high-resolution studies. In particular new, low-amplitude compact sensors, such as the quartz tuning fork [239] or the length-extension-resonator [240], appear as very promising alternatives to the conventional cantilever based microscopes for liquid phase NC-AFM. Although the liquid phase NC-AFM will likely have the greatest impact on the biological sciences [89, 233], a further breakthrough in high-resolution FM-mode NC-AFM would also open up many new exciting applications in the context of metal oxide surface science, such as in heterogeneous catalysis, electro-chemistry and mineralogy where metal oxides play an extremely important role.

Acknowledgments

JVL would like to thank the colleagues and co-workers on this project at iNANO and Haldor Topsøe A/S. JVL gratefully acknowledges R Bechstein, G H Enevoldsen, M K Rasmussen, K Venkataramani, M C Christensen and F Besenbacher for input to this review. M C Christensen is further acknowledged for providing the unpublished work on the O-terminated ZnO surface. JVL also gratefully acknowledge Adam S Foster for a fruitful collaboration. JVL acknowledges generous support from the Lundbeck Foundation, the European Research Council (ERC Starting Independent Researcher Grant #239834) and Haldor Topsøe A/S. MR gratefully acknowledges the contributions from S Gritschneder, F Ostendorf and S Torbrügge to this review, most fruitful discussions on oxide issues and collaboration with F Besenbacher, Ó Custance, F Esch, S Fabris, A S Foster, V Ganduglia-Pirovano, P Luches, G Kresse, A Kühnle, B Meyer, R Pérez, H H Pieper, M Schmid, A L Shluger, F Träger, P Varga, S Valeri, Y Wang, C Wöll and financial support by the Deutsche Forschungsgemeinschaft.

References

[1] Fierro J L G (ed) 2006 *Metal Oxides—Chemistry and Applications* (Boca Raton, FL: Taylor and Francis)
[2] Rao C N R and Rayeau B 1998 *Transition Metal Oxides: Structure, Properties, and Synthesis of Ceramic Oxides* (New York: Wiley)
[3] Henrich V E and Cox P A 1996 *The Surface Science of Metal Oxides* (Cambridge: Cambridge University Press)
[4] Kaneko M and Okura I (ed) 2002 *Photocatalysis—Science and Technology* (Berlin: Springer)
[5] Ellmer K, Klein A and Rech B (ed) 2008 *Transparent Conductive Zinc Oxide: Basics and Applications in Thin Film Solar Cells* (Berlin: Springer)
[6] Pan Z W, Dai Z R and Wang Z L 2001 *Science* **291** 1947–9
[7] Schmidt-Mende L and MacManus-Driscoll J L 2007 *Mater. Today* **10** 40–8
[8] Wang Z L 2004 *J. Phys.: Condens. Matter* **16** R829–58

[9] Henrich V E 2001 *Oxide Surfaces* ed D P Woodruff (Amsterdam: Elsevier Science) pp 1–34
[10] Bonnell D A and Garra J 2008 *Rep. Prog. Phys.* **71** 044501
[11] Bonnell D A 2001 *Scanning Tunneling Microscopy and Spectroscopy* (New York: Wiley–VCH)
[12] Freund H J and Pacchioni G 2008 *Chem. Soc. Rev.* **37** 2224–42
[13] Schmid M, Kresse G, Buchsbaum A, Napetschnig E, Gritschneder S, Reichling M and Varga P 2007 *Phys. Rev. Lett.* **99** 196104
[14] Kresse G, Schmid M, Napetschnig E, Shishkin M, Kohler L and Varga P 2005 *Science* **308** 1440–2
[15] Sterrer M, Risse T, Heyde M, Rust H P and Freund H J 2007 *Phys. Rev. Lett.* **98** 206103
[16] Hellman A and Grönbeck H 2008 *Phys. Rev. Lett.* **100** 4
[17] Giessibl F J 2003 *Rev. Mod. Phys.* **75** 949–83
[18] Morita S, Wiesendanger R and Meyer E 2002 *Noncontact Atomic Force Microscopy* (New York: Springer)
[19] Custance Ó, Pérez R and Morita S 2009 *Nat. Nanotechnol.* **4** 803–10
[20] Morita S, Giessibl F J and Wiesendanger R (ed) 2009 *Noncontact Atomic Force Microscopy* vol 2 (Berlin: Springer)
[21] Barth C and Reichling M 2001 *Nature* **414** 54–7
[22] Giessibl F J 1995 *Science* **267** 68–71
[23] Fukui K-i, Onishi H and Iwasawa Y 1997 *Phys. Rev. Lett.* **79** 4202–5
[24] Fukui K-i, Onishi H and Iwasawa Y 1997 *Chem. Phys. Lett.* **280** 296–301
[25] Fukui K-i, Onishi H and Iwasawa Y 1999 *Appl. Surf. Sci.* **140** 259–64
[26] Raza H, Pang C L, Haycock S A and Thornton G 1998 *Appl. Surf. Sci.* **140** 271–5
[27] Lauritsen J V, Foster A S, Olesen G H, Christensen M C, Kühnle A, Helveg S, Rostrup-Nielsen J R, Clausen B S, Reichling M and Besenbacher F 2006 *Nanotechnology* **17** 3436–41
[28] Sasahara A, Pang C L and Onishi H 2006 *J. Phys. Chem.* B **110** 13453–7
[29] Pang C L, Sasahara A, Onishi H, Chen Q and Thornton G 2006 *Phys. Rev.* B **74** 073411
[30] Enevoldsen G H, Foster A S, Christensen M C, Lauritsen J V and Besenbacher F 2007 *Phys. Rev.* B **76** 205415
[31] Enevoldsen G H, Glatzel T, Christensen M C, Lauritsen J V and Besenbacher F 2008 *Phys. Rev. Lett.* **100** 236104
[32] Enevoldsen G H, Pinto H P, Foster A S, Jensen M C R, Kühnle A, Reichling M, Hofer W A, Lauritsen J V and Besenbacher F 2008 *Phys. Rev.* B **78** 045416
[33] Enevoldsen G H, Pinto H P, Foster A S, Jensen M C R, Hofer W A, Hammer B, Lauritsen J V and Besenbacher F 2009 *Phys. Rev. Lett.* **102** 136103
[34] Pang C L, Muryn C A, Woodhead A P, Raza H, Haycock S A, Dhanak V R and Thornton G 2005 *Surf. Sci.* **583** L147–52
[35] Sasahara A, Kitamura S, Uetsuka H and Onishi H 2004 *J. Phys. Chem.* B **108** 15735–7
[36] Sasahara A, Uetsuka H and Onishi H 2003 *Surf. Sci.* **529** L245–50
[37] Namai Y and Matsuoka O 2005 *J. Phys. Chem.* B **109** 23948–54
[38] Iwasawa Y, Onishi H, Fukui K-i, Suzuki S and Sasaki T 1999 *Faraday Discuss.* **114** 259–66
[39] Bechstein R, Gonzalez C, Schütte J, Jelinek P, Pérez R and Kühnle A 2009 *Nanotechnology* **20** 505703
[40] Pang C L, Raza H, Haycock S A and Thornton G 1999 *Appl. Surf. Sci.* **157** 233–8
[41] Ashino M, Sugawara Y, Morita S and Ishikawa M 2001 *Phys. Rev. Lett.* **86** 4334–7
[42] Ashino M, Uchihashi T, Yokoyama K, Sugawara Y, Morita S and Ishikawa M 2000 *Phys. Rev.* B **61** 13955–9
[43] Kubo T, Orita H and Nozoye H 2007 *J. Am. Chem. Soc.* **129** 10474–8
[44] Wang J, Howard A, Egdell R G, Pethica J B and Foord J S 2002 *Surf. Sci.* **515** 337–43
[45] Lauritsen J V, Jensen M C R, Venkataramani K, Hinnemann B, Helveg S, Clausen B S and Besenbacher F 2009 *Phys. Rev. Lett.* **103** 076103
[46] Sasahara A, Uetsuka H and Onishi K 2000 *Japan. J. Appl. Phys.* 1 **39** 3773–6
[47] Hamm G, Barth C, Becker C, Wandelt K and Henry C R 2006 *Phys. Rev. Lett.* **97** 126106
[48] Gritschneder S, Becker C, Wandelt K and Reichling M 2007 *J. Am. Chem. Soc.* **129** 4925–8
[49] Pang C L, Raza H, Haycock S A and Thornton G 2002 *Phys. Rev.* B **65** 201401
[50] Simon G H, König T, Nilius M, Rust H P, Heyde M and Freund H J 2008 *Phys. Rev.* B **78** 113401
[51] Simon G H, König T, Rust H P, Heyde M and Freund H J 2009 *New J. Phys.* **11** 093009
[52] Ostendorf F, Torbrügge S and Reichling M 2008 *Phys. Rev.* B **77** 041405
[53] Torbrügge S, Ostendorf F and Reichling M 2009 *J. Phys. Chem.* C **113** 4909–14
[54] Jensen M C R 2008 Atomic-scale characterization of Al_2O_3, ZnO and TiO_2 surfaces *PhD Thesis* Aarhus University, Aarhus
[55] Fukui K-i, Namai Y and Iwasawa Y 2001 *Appl. Surf. Sci.* **188** 252–6
[56] Namai Y, Fukui K-i and Iwasawa Y 2003 *Catal. Today* **85** 79–91
[57] Namai Y, Fukui K-i and Iwasawa Y 2003 *J. Phys. Chem.* B **107** 11666–73
[58] Gritschneder S, Namai Y, Iwasawa Y and Reichling M 2005 *Nanotechnology* **16** S41–8
[59] Gritschneder S, Iwasawa Y and Reichling M 2007 *Nanotechnology* **18** 044025
[60] Gritschneder S and Reichling M 2007 *Nanotechnology* **18** 044025
[61] Torbrügge S, Reichling M, Ishiyama A, Morita S and Custance O 2007 *Phys. Rev. Lett.* **99** 056101
[62] Gritschneder S and Reichling M 2008 *J. Phys. Chem.* C **112** 2045–9
[63] Namai Y, Fukui K-i and Iwasawa Y 2004 *Nanotechnology* **15** S49
[64] Namai Y, Fukui K-i and Iwasawa Y 2003 *J. Phys. Chem.* B **107** 11666–73
[65] Fukui K-i and Iwasawa Y 1999 *Surf. Sci.* **441** 529–41
[66] Ashworth T V, Pang C L, Wincott P L, Vaughan D J and Thornton G 2003 *Appl. Surf. Sci.* **210** 2–5
[67] Barth C and Henry C R 2003 *Phys. Rev. Lett.* **91** 196102
[68] Heyde M, Sterrer M, Rust H P and Freund H J 2005 *Appl. Phys. Lett.* **87** 083104
[69] Heyde M, Simon G H, Rust H P and Freund H J 2006 *Appl. Phys. Lett.* **89** 263107
[70] Heyde M, Sterrer M, Rust H P and Freund H J 2006 *Nanotechnology* **17** S101–6
[71] Kubo T and Nozoye H 2001 *Appl. Phys.* A **72** S277–80
[72] Kubo T and Nozoye H 2001 *Phys. Rev. Lett.* **86** 1801–4
[73] Pang C L, Haycock S A, Raza H, Møller P J and Thornton G 2000 *Phys. Rev.* B **62** R7775–8
[74] Schwarz A, Hölscher H, Langkat S M and Wiesendanger R 2003 *Scanning Tunneling Microscopy/Spectroscopy and Related Techniques* vol 696 pp 68–78
[75] Hosoi H, Sueoka K, Hayakawa K and Mukasa K 2000 *Appl. Surf. Sci.* **157** 218–21
[76] Hosoi H, Kimura M, Hayakawa K, Sueoka K and Mukasa K 2001 *Appl. Phys.* A **72** S23–6

[77] Kaiser U, Schwarz A and Wiesendanger R 2007 *Nature* **446** 522–5
[78] Schmid M, Mannhart J and Giessibl F J 2008 *Phys. Rev.* B **77** 045402
[79] Allers W, Langkat S and Wiesendanger R 2001 *Appl. Phys.* A **72** S27–30
[80] Suzuki S, Ohminami Y, Tsutsumi T, Shoaib M M, Ichikawa M and Asakura K 2003 *Chem. Lett.* **32** 1098–9
[81] Kubo T and Nozoye H 2002 *Appl. Surf. Sci.* **188** 545–9
[82] Ostendorf F, Schmitz C, Hirth S, Kühnle A, Kolodziej J J and Reichling M 2009 *Langmuir* **25** 10764–7
[83] Sasahara A, Droubay T C, Chambers S A, Uetsuka H and Onishi H 2005 *Nanotechnology* **16** S18–21
[84] Ostendorf F, Schmitz C, Hirth S, Kühnle A, Kolodziej J J and Reichling M 2008 *Nanotechnology* **19** 305705
[85] Binning G, Rohrer H, Gerber C and Weibel E 1982 *Phys. Rev. Lett.* **49** 57–61
[86] Nonnenmacher M, O'Boyle M P and Wickramasinghe H K 1991 *Appl. Phys. Lett.* **58** 2921–3
[87] García R and Pérez R 2002 *Surf. Sci. Rep.* **47** 197–301
[88] Morris V J, Gunning A P and Kirby A R 1999 *Atomic Force Microscopy for Biologists* (London: Imperial College Press)
[89] Amrein M 2007 *Science of Microscopy* ed P W Hawkes and J C H Spence (New York: Springer) pp 1025–69
[90] Nikiforov M P and Bonnell D A 2007 *Science of Microscopy* ed P W Hawkes and J C H Spence (New York: Springer) pp 929–68
[91] Hirth S, Ostendorf F and Reichling M 2006 *Nanotechnology* **17** S148–54
[92] Hofer W A, Foster A S and Shluger A L 2003 *Rev. Mod. Phys.* **75** 1287–331
[93] Arai T and Tomitori M 2000 *Appl. Surf. Sci.* **157** 207–11
[94] Hoffmann R, Kantorovich L N, Baratoff A, Hug H J and Güntherodt H J 2004 *Phys. Rev. Lett.* **92** 146103
[95] Foster A S, Barth C and Henry C R 2009 *Phys. Rev. Lett.* **102** 256103
[96] Foster A S, Barth C, Shluger A L and Reichling M 2001 *Phys. Rev. Lett.* **86** 2373–6
[97] Barth C, Foster A S, Reichling M and Shluger A L 2001 *J. Phys.: Condens. Matter* **13** 2061–79
[98] Hoffmann R, Barth C, Foster A S, Shluger A L, Hug H J, Güntherodt H J, Nieminen R M and Reichling M 2005 *J. Am. Chem. Soc.* **127** 17863–6
[99] Foster A S, Shluger A L and Nieminen R M 2004 *Nanotechnology* **15** S60
[100] Foster A S, Hofer W A and Shluger A L 2001 *Curr. Opin. Solid State Mater. Sci.* **5** 427–34
[101] Foster A S, Shluger A L and Nieminen R M 2002 *Appl. Surf. Sci.* **188** 306–18
[102] Heinrich V E and Cox P A 1994 *The Surface Science of Metal Oxides* (Cambridge: Cambridge University Press)
[103] Wang X G, Chaka A and Scheffler M 2000 *Phys. Rev. Lett.* **84** 3650–3
[104] Kresse G, Dulub O and Diebold U 2003 *Phys. Rev.* B **68** 245409
[105] Wang X-G, Weiss W, Shaikhutdinov S K, Ritter M, Petersen M, Wagner F, Schlögl R and Scheffler M 1998 *Phys. Rev. Lett.* **81** 1038–42
[106] Diebold U, Pan J-M and Madey T E 1995 *Surf. Sci.* **331–333** 845–54
[107] Barth C, Claeys C and Henry C R 2005 *Rev. Sci. Instrum.* **76** 083907
[108] Schmid M, Renner A and Giessibl F J 2006 *Rev. Sci. Instrum.* **77** 036101
[109] Tröger L, Schutte J, Ostendorf F, Kühnle A and Reichling M 2009 *Rev. Sci. Instrum.* **80** 063703
[110] Linsebigler A, Lu G and Yates J T J 1995 *Chem. Rev.* **95** 735–58
[111] Irie H, Sunada K and Hashimoto K 2004 *Electrochemistry* **72** 807–12
[112] Haruta M 1997 *Catal. Today* **36** 153–66
[113] Valden M, Lai X and Goodman D W 1998 *Science* **281** 1647–50
[114] Diebold U 2003 *Surf. Sci. Rep.* **48** 53–229
[115] Pang C L, Bikondoa O, Humphrey D S, Papageorgiou A C, Cabailh G, Ithnin R, Chen Q, Muryn C A, Onishi H and Thornton G 2006 *Nanotechnology* **17** 5397–405
[116] Wendt S, Schaub R, Matthiesen J, Vestergaard E, Wahlström E, Rasmussen M D, Thostrup P, Molina L M, Lægsgaard E, Stensgaard I, Hammer B and Besenbacher F 2005 *Surf. Sci.* **598** 226–45
[117] Ke S H, Uda T and Terakura K 2002 *Appl. Surf. Sci.* **188** 319–24
[118] Foster A S, Pakarinen O H, Airaksinen J M, Gale J D and Nieminen R M 2003 *Phys. Rev.* B **68** 195410
[119] Diebold U 2001 *Oxide Surfaces* ed D P Woodruff (Amsterdam: Elsevier Science) pp 443–84
[120] Wendt S, Matthiesen J, Schaub R, Vestergaard E K, Lægsgaard E, Besenbacher F and Hammer B 2006 *Phys. Rev. Lett.* **96** 066107
[121] Bikondoa O, Pang C L, Ithnin R, Muryn C A, Onishi H and Thornton G 2006 *Nat. Mater.* **5** 189–92
[122] Henderson M A 1996 *Surf. Sci.* **355** 151–66
[123] Gross L, Mohn F, Liljeroth P, Repp J, Giessibl F J and Meyer G 2009 *Science* **324** 1428–31
[124] Foster A S, Gal A Y, Nieminen R M and Shluger A L 2005 *J. Phys. Chem.* B **109** 4554–60
[125] Rahe P, Bechstein R, Schütte J, Ostendorf F and Kühnle A 2008 *Phys. Rev.* B **77** 195410
[126] Pang C L and Thornton G 2006 *Surf. Sci.* **600** 4405–6
[127] Wefers K and Chanakya M 1987 *Oxides and Hydroxides of Aluminum* Alcoa Laboratories
[128] Chang C C 1968 *J. Appl. Phys.* **39** 5570
[129] French T M and Somorjai G A 1970 *J. Phys. Chem.* **74** 2489–96
[130] Toofan J and Watson P R 1998 *Surf. Sci.* **401** 162–72
[131] Renaud G, Villette B, Vilfan I and Bourret A 1994 *Phys. Rev. Lett.* **73** 1825–8
[132] Ahn J and Rabalais J W 1997 *Surf. Sci.* **388** 121–31
[133] Gautier M, Renaud G, Van L P, Villette B, Pollak M, Thromat N, Jollet F and Duraud J P 1994 *J. Am. Ceram. Soc.* **77** 323–34
[134] Hass K C, Schneider W F, Curioni A and Andreoni W 2000 *J. Phys. Chem.* B **104** 5527–40
[135] Hass K C, Schneider W F, Curioni A and Andreoni W 1998 *Science* **282** 265–8
[136] Eng P J, Trainor T P, Brown G E, Waychunas G A, Newville M, Sutton S R and Rivers M L 2000 *Science* **288** 1029–33
[137] Hinnemann B and Carter E A 2007 *J. Phys. Chem.* C **111** 7105–26
[138] Lodziana Z, Nørskov J K and Stoltze P 2003 *J. Chem. Phys.* **118** 11179–88
[139] Lodziana Z and Nørskov J K 2002 *Surf. Sci.* **518** L577–82
[140] Lodziana Z and Nørskov J K 2001 *J. Chem. Phys.* **115** 11261–7
[141] Kelber J A 2007 *Surf. Sci. Rep.* **62** 271–303
[142] Vilfan I, Deutsch T, Lancon F and Renaud G 2002 *Surf. Sci.* **505** L215–21
[143] Vermeersch M, Sporken R, Lambin P and Caudano R 1990 *Surf. Sci.* **235** 5–14
[144] Jarvis E A A and Carter E A 2001 *J. Phys. Chem.* B **105** 4045–52

[145] Vilfan I, Lancon F and Villain J 1997 *Surf. Sci.* **392** 62–8
[146] Barth C and Reichling M 2002 *Noncontact Atomic Force Microscopy* ed S Morita *et al* (Berlin: Springer) pp 135–45
[147] Jensen M C R, Venkataramani K, Helveg S, Clausen B S, Reichling M, Besenbacher F and Lauritsen J V 2008 *J. Phys. Chem.* C **112** 16953–60
[148] Gan Y and Franks G V 2005 *J. Phys. Chem.* B **109** 12474–9
[149] Wang Z L and Song J H 2006 *Science* **312** 242–6
[150] Goniakowski J, Finocchi F and Noguera C 2008 *Rep. Prog. Phys.* **71** 016501
[151] Tasker P W 1979 *J. Phys. C: Solid State Phys.* **12** 4977–84
[152] Noguera C 2000 *J. Phys.: Condens. Matter* **12** R367–410
[153] Wöll C 2007 *Prog. Surf. Sci.* **82** 55–120
[154] Dulub O, Boatner L A and Diebold U 2002 *Surf. Sci.* **519** 201–17
[155] Meyer B and Marx D 2003 *Phys. Rev.* B **67** 035403
[156] Meyer B 2004 *Phys. Rev.* B **69** 045416
[157] Wander A, Schedin F, Steadman P, Norris A, McGrath R, Turner T S, Thornton G and Harrison N M 2001 *Phys. Rev. Lett.* **86** 3811–4
[158] Valtiner M, Todorova M, Grundmeier G and Neugebauer J 2009 *Phys. Rev. Lett.* **103** 065502
[159] Lindsay R, Muryn C A, Michelangeli E and Thornton G 2004 *Surf. Sci.* **565** L283–7
[160] Overbury S H, Radulovic P V, Thevuthasan S, Herman G S, Henderson M A and Peden C H F 1998 *Surf. Sci.* **410** 106–22
[161] Jedrecy N, Sauvage-Simkin M and Pinchaux R 2000 *Appl. Surf. Sci.* **162** 69–73
[162] Dulub O, Diebold U and Kresse G 2003 *Phys. Rev. Lett.* **90** 016102
[163] King S T, Parihar S S, Pradhan K, Johnson-Steigelman H T and Lyman P F 2008 *Surf. Sci.* **602** L131–4
[164] Dumont J, Hackens B, Faniel S, Mouthuy P O, Sporken R and Melinte S 2009 *Appl. Phys. Lett.* **95** 132102
[165] Kunat M, Gil Girol S, Becker T, Burghaus U and Wöll C 2002 *Phys. Rev.* B **66** 081402
[166] Lindsay R, Michelangeli E, Daniels B G, Ashworth T V, Limb A J, Thornton G, Gutierrez-Sosa A, Baraldi A, Larciprete R and Lizzit S 2002 *J. Am. Chem. Soc.* **124** 7117–22
[167] Jensen M C R, Rasmussen M K and Lauritsen J V 2009 unpublished
[168] Trovarelli A, de Leitenburg C, Boaro M and Dolcetti G 1999 *Catal. Today* **50** 353–67
[169] Trovarelli A 1996 *Catal. Rev.-Sci. Eng.* **38** 439–520
[170] Mamontov E, Egami T, Brezny R, Koranne M and Tyagi S 2000 *J. Phys. Chem.* B **104** 11110–6
[171] Skorodumova N V, Simak S I, Lundqvist B I, Abrikosov I A and Johansson B 2002 *Phys. Rev. Lett.* **89** 166601
[172] Fu Q, Saltsburg H and Flytzani-Stephanopoulos M 2003 *Science* **301** 935–8
[173] Aneggi E, Boaro M, de Leitenburg C, Dolcetti G and Trovarelli A 2006 *J. Alloys Compounds* **408** 1096–102
[174] Huang M and Fabris S 2007 *Phys. Rev.* B **75** 081404
[175] Gandhi H S, Graham G W and McCabe R W 2003 *J. Catal.* **216** 433–42
[176] Shelef M, Graham G W and McCabe R W 2002 *Catalytic Science Series* ed A Trovarelli (London: Imperial College Press) p 343
[177] Henderson M A, Perkins C L, Engelhard M H, Thevuthasan S and Peden C H F 2003 *Surf. Sci.* **526** 1–18
[178] Martínez-Arias A, Hungría A B, Fernández-García M, Conesa J C and Munuera G 2004 *J. Phys. Chem.* B **108** 17983–91
[179] Pillai U R and Deevi S 2006 *Appl. Catal.* A **299** 266–73
[180] Teschner D, Wootsch A, Pozdnyakova O, Sauer H, Knop-Gericke A and Schlögl R 2006 *React. Kinet. Catal. Lett.* **87** 235–47
[181] Deng W L, Carpenter C, Yi N and Flytzani-Stephanopoulos M 2007 *Top. Catal.* **44** 199–208
[182] Fu Q, Kudriavtseva S, Saltsburg H and Flytzani-Stephanopoulos M 2003 *Chem. Eng. J.* **93** 41–53
[183] Fu Q, Weber A and Flytzani-Stephanopoulos M 2001 *Catal. Lett.* **77** 87–95
[184] Jacobs G, Ricote S and Davis B H 2006 *Appl. Catal.* A **302** 14–21
[185] Rodriguez J A, Ma S, Liu P, Hrbek J, Evans J and Pérez M 2007 *Science* **318** 1757–60
[186] Deng W, Frenkel A I, Si R and Flytzani-Stephanopoulos M 2008 *J. Phys. Chem.* C **112** 12834–40
[187] Li L, Zhan Y Y, Zheng Q, Zheng Y H, Chen C Q, She Y S, Lin X Y and Wei K M 2009 *Catal. Lett.* **130** 532–40
[188] Liu X W, Zhou K B, Wang L, Wang B Y and Li Y D 2009 *J. Am. Chem. Soc.* **131** 3140–9
[189] Baron M, Bondarchuk O, Stacchiola D, Shaikhutdinov S and Freund H J 2009 *J. Phys. Chem.* C **113** 6042–9
[190] Majimel J, Lamirand-Majimel M, Moog I, Feral-Martin C and Tréguer-Delapierre M 2009 *J. Phys. Chem.* C **113** 9275–83
[191] Skoda M, Cabala M, Matolinova I, Prince K C, Skala T, Sutara F, Veltruska K and Matolin V 2009 *J. Chem. Phys.* **130** 034703
[192] Yang Z X, Woo T K, Baudin M and Hermansson K 2004 *J. Chem. Phys.* **120** 7741–9
[193] Yang Z X, Woo T K and Hermansson K 2004 *Chem. Phys. Lett.* **396** 384–92
[194] Fabris S, Vicario G, Balducci G, de Gironcoli S and Baroni S 2005 *J. Phys. Chem.* B **109** 22860–7
[195] Herschend B, Baudin M and Hermansson K 2006 *Chem. Phys.* **328** 345–53
[196] Nolan M and Watson G W 2006 *J. Phys. Chem.* B **110** 16600–6
[197] Fronzi M, Soon A, Delley B, Traversa E and Stampfl C 2009 *J. Chem. Phys.* **131** 16
[198] Conesa J C 2009 *Catal. Today* **143** 315–25
[199] Zhang C J, Michaelides A, King D A and Jenkins S J 2009 *Phys. Rev.* B **79** 075433
[200] Castellani N J, Branda M A, Neyman K M and Illas F 2009 *J. Phys. Chem.* C **113** 4948–54
[201] Hernández N C, Grau-Crespo R, de Leeuw N H and Sanz J F 2009 *Phys. Chem. Chem. Phys.* **11** 5246–52
[202] Zhang C J, Michaelides A, King D A and Jenkins S J 2009 *J. Phys. Chem.* C **113** 6411–7
[203] Liu Z P, Jenkins S J and King D A 2005 *Phys. Rev. Lett.* **94** 196102
[204] Nolan M, Parker S C and Watson G W 2006 *Phys. Chem. Chem. Phys.* **8** 216–8
[205] Esch F, Fabris S, Zhou L, Montini T, Africh C, Fornasiero P, Comelli G and Rosei R 2005 *Science* **309** 752–5
[206] Nörenberg H and Briggs G A D 1997 *Phys. Rev. Lett.* **79** 4222–5
[207] Torbrügge S, Lübbe J, Tröger L, Cranney M, Eguchi T, Hasegawa Y and Reichling M 2008 *Rev. Sci. Instrum.* **79** 083701
[208] Torbrügge S, Cranney M and Reichling M 2008 *Appl. Phys. Lett.* **93** 073112
[209] Ganduglia-Pirovano M V, Da Silva J L F and Sauer J 2009 *Phys. Rev. Lett.* **102** 026101
[210] Kantorovich L N and Trevethan T 2004 *Phys. Rev. Lett.* **93** 236102
[211] Oyabu N, Pou P, Sugimoto Y, Jelinek P, Abe M, Morita S, Pérez R and Custance Ó 2006 *Phys. Rev. Lett.* **96** 106101
[212] Ertl G, Knözinger H and Weitkamp J (ed) 1997 *Handbook of Heterogeneous Catalysis* vol 1–5 (Weinheim: VCH)
[213] Matthey D, Wang J G, Wendt S, Matthiesen J, Schaub R, Lægsgaard E, Hammer B and Besenbacher F 2007 *Science* **315** 1692–6

[214] Hansen P L, Wagner J B, Helveg S, Rostrup-Nielsen J R, Clausen B S and Topsøe H 2002 *Science* **295** 2053–5
[215] Zhadanov V P and Kasemo B 1998 *Phys. Rev. Lett.* **81** 2482–5
[216] Conner W C and Falconer J L 1995 *Chem. Rev.* **95** 759–88
[217] Henry C R 1998 *Surf. Sci. Rep.* **31** 231–325
[218] Freund H-J 2002 *Surf. Sci.* **500** 271–99
[219] Bäumer M and Freund H-J 1999 *Prog. Surf. Sci.* **61** 127–98
[220] Lauritsen J V and Besenbacher F 2006 *Adv. Catal.* **50** 97–143
[221] Dulub O, Batzill M and Diebold U 2005 *Top. Catal.* **36** 65–76
[222] Lai X, St Clair T P, Valden M and Goodman D W 1998 *Prog. Surf. Sci.* **59** 25–52
[223] Tait S L, Ngo L T, Yu Q M, Fain S C and Campbell C T 2005 *J. Chem. Phys.* **122** 064712
[224] Pang C L, Ashworth T V, Raza H, Haycock S A and Thornton G 2004 *Nanotechnology* **15** 862–6
[225] Pang C L, Raza H, Haycock S A and Thornton G 2000 *Surf. Sci.* **460** L510–4
[226] Pakarinen O H, Barth C, Foster A S and Henry C R 2008 *J. Appl. Phys.* **103** 054313
[227] Barth C and Henry C R 2009 *J. Phys. Chem.* C **113** 247–53
[228] Liang G and Perry S S 2005 *Surf. Sci.* **594** 132–40
[229] Barth C, Pakarinen O H, Foster A S and Henry C R 2006 *Nanotechnology* **17** S128–36
[230] Bäumer M and Freund H J 1999 *Prog. Surf. Sci.* **61** 127–98
[231] Hansen K H, Worren T, Stempel S, Lægsgaard E, Bäumer M, Freund H J, Besenbacher F and Stensgaard I 1999 *Phys. Rev. Lett.* **83** 4120–3
[232] Worren T, Hansen K H, Lægsgaard E, Besenbacher F and Stensgaard I 2001 *Surf. Sci.* **477** 8–16
[233] Hogan J 2006 *Nature* **440** 14–5
[234] Fukuma T, Kimura K, Kobayashi K, Matsushige K and Yamada H 2005 *Rev. Sci. Instrum.* **76** 126110
[235] Hoogenboom B W, Frederix P, Yang J L, Martin S, Pellmont Y, Steinacher M, Zach S, Langenbach E and Heimbeck H J 2005 *Appl. Phys. Lett.* **86** 074101
[236] Fukuma T, Kobayashi K, Matsushige K and Yamada H 2005 *Appl. Phys. Lett.* **87** 034101
[237] Fukuma T, Higgins M J and Jarvis S P 2007 *Phys. Rev. Lett.* **98** 106101
[238] Rode S, Oyabu N, Kobayashi K, Yamada H and Kühnle A 2009 *Langmuir* **25** 2850–3
[239] Giessibl F J 2000 *Appl. Phys. Lett.* **76** 1470–2
[240] An T, Eguchi T, Akiyama K and Hasegawa Y 2006 *Appl. Phys. Lett.* **88** 133114